Department of Physics and Astronomy
University of Heidelberg

Master Thesis
in Physics
submitted by

Michael Karl Rosner

born in Marktredwitz (Germany)

2019

Production and preparation of highly charged ions for re-trapping in ultra-cold environments

This Master Thesis has been carried out by Michael Karl Rosner at the
Max-Planck-Institut für Kernphysik (MPIK) in Heidelberg
under the supervision of
Priv.-Doz. Dr. José Ramón Crespo López-Urrutia

Abstract

Certain highly charged ions (HCIs) exhibit enhanced sensitivity to fundamental interactions due to the specifics of their level structure, enabling improvement in atomic clocks and frequency metrology. This allows more precise tests of fundamental physics than achievable with atoms or singly charged ions, e. g. in the search for a possible time variation of the fine-structure constant α. Their narrow optical transitions make them suitable targets for quantum metrology, as recently demonstrated for Ar^{13+}. An electron beam ion trap (EBIT) is used to produce ions in the desired charge states. However, the high temperature within EBITs requires a transfer of the HCIs into a cooling trap to perform high-resolution spectroscopy. This work presents a setup comprising an EBIT and a beamline suitable for transfer, bunching, precooling and deceleration of extracted HCIs. In the EBIT, an electron beam is electrically accelerated and magnetically compressed to sequentially ionize neutral atoms injected into the trap center to generate HCIs. The ion optics, diagnostic elements and a decelerating/pre-cooling unit of the beamline prepare them for re-trapping. Time-of-flight measurements were performed to determine the charge state distribution of the extracted ions. Furthermore, a retarding field analyzer allowed the determination of their mean kinetic energy as well as their energy spread, which has been subsequently reduced in the pre-cooling unit.

Zusammenfassung

Bestimmte hochgeladene Ionen (HCI) zeigen, aufgrund der Besonderheiten ihrer Energieniveaustruktur, eine erhöhte Sensibilität gegenüber fundamentalen Interaktionen, was Verbesserungen von Atomuhren sowie Frequenzmetrologie ermöglicht. Dies gestattet genauere Untersuchungen fundamentaler Physik als mit Atomen oder einfach geladenen Ionen, beispielsweise bei der Suche nach möglichen zeitlichen Schwankungen der Feinstrukturkonstante α. Mögliche schmale optische Übergänge machen sie zu geeigneten Kandidaten für Quantenmetrologie, wie kürzlich an Ar^{13+} gezeigt. Eine Elektronenstrahl-Ionenfalle (EBIT) wird verwendet, um Ionen im gewünschten Ladungszustand zu erzeugen. Aufgrund der hohen Temperatur innerhalb EBITs ist allerdings der Transfer in eine Kühlfalle notwendig, um hochaufgelöste Spektroskopie zu betreiben. In dieser Arbeit wird ein Aufbau aus EBIT und Strahlrohr, das zum Transfer, Bündeln, Vorkühlen und Abbremsen geeignet ist, präsentiert. In der EBIT wird ein Elektronenstrahl beschleunigt und magnetisch komprimiert, um neutrale, ins Fallenzentrum injizierte, Atome sequenziell zu ionisieren und so HCIs zu generieren. Die Ionenoptiken, Diagnoseelemente und eine Abbrems-/Vorkühleinheit des Strahlrohrs bereiten diese auf ein Wiedereinfangen vor. Die Ladungszustandsverteilung der extrahierten Ionen wurde durch Flugzeitmessungen bestimmt. Außerdem wurde mit der Gegenfeldmethode ihre kinetische Energie sowie Energieverteilung gemessen und anschließend innerhalb der Vorkühleinheit verringert.

Contents

Acronyms

CHX

charge exchange.

DT

drift tube.

EBIT

electron beam ion trap.

EIE

electron impact excitation.

EII

electron impact ionization.

HCI

highly charged ion.

MCP

microchannel plate.

PDT

pulsed drift tube.

PEEK

polyether ether ketone.

RR

radiative recombination.

SL

Sikler lens.

ToF

time of flight.

UHV

ultra-high vacuum.

Chapter 1

Introduction

> "In our highly complex and ever changing world it is reassuring to know that certain physical quantities can be measured and predicted with very high precision. Precision measurements have always appealed to me as one of the most beautiful aspects of physics. With better measuring tools, one can look where no one has looked before. More than once, seemingly minute differences between measurement and theory have led to major advances in fundamental knowledge. The birth of modern science itself is intimately linked to the art of accurate measurements."
> — Theodor W. Hänsch [1]

Theories in physics are not particularly useful unless they provide predictions about measurable quantities, which can be subsequently verified utilizing a suitable experiment [2]. These physical quantities are usually expressed by a numerical value, representing the magnitude, and a unit of measurement, giving the reference to which the new measurement is compared. While the history of measurements dates as far back as to the ancient Egyptians in 2900 BC, it took a few more millennia until in 1668 a common measurement system as a universal language was proposed [3].
The astronomically defined "second" became the basis for this system. The length of a pendulum with a period of 2 seconds, $\sim 994\,\mathrm{mm}$, the "standard", was defined. This was a remarkable step since lengths could be now expressed with the help of time scales in a more or less reproducible way. The unit of mass, the "hundred", was linked to the standard via the density of distilled rainwater. [4]

The first international recognition of a standardized system took place two hundred years later when 17 nations signed the *Convention du Mètre* on May 20$^{\text{th}}$, 1878, where physical representations of the "meter" for lengths and "kilogram" for masses were introduced as a reference. A unit of time, the "second", was added as 1/86400 of a mean solar day, which was later found to be varying and therefore unreliable. With the time evolving, deviations of the physical prototype kilograms and meter were also discovered. [5]
Atomic standards of time have proven to be reliable and reproducible reference frames: The ground state hyperfine transition in cesium 133 replaced the astronomical definition of the second. With this new definition, the system changed its name to *Système international d'unités* - the SI system. The new definition of the second proved so reliable, that it was used as a reference for other SI units as well: In 1983, the meter was defined as a fixed fraction of the length light travels in a second, setting the vacuum velocity of light to a fixed value. In 2018, Planck's constant was set to a fixed value as well, defining the kilogram based on the second as well. Additionally, the elementary charge was fixed, now linking the "ampere" to the second as well. Defining a fixed value for Boltzmann's constant, linking temperature to energy - a combination of length, time and mass - also referenced the "kelvin" on the definition of time. This leaves only two of seven SI units not depending on an accurate measurement of time: The "candela", measuring the luminous intensity, and the "mole", measuring the amount of a substance. [6]
This dependency of most unit definitions on the accurate measurement of time has a simple reason: Time, more precise its reciprocal, frequency, is the quantity we can measure with the highest precision, and has been so for quite a while [1]. The first clock with such unequivocal precision was the pendulum clock build by Christian Huygens in 1657, based on an idea of Galileo Galilei [7]. A century later a famous comparison between an accurate clock and other methods of measurement took place: While most scientists at the time looked for an astronomical solution for the problem of determining the longitude at sea, the English clockmaker John Harrison came up with a more simpler and practical answer - building the first maritime chronometer [8].
The advancement of clocks continued rapidly, changing from mechanical pendula to electric oscillators at the beginning of the 20th century, stabilizing time to the piezoelectric vibration of quartz crystals [7]. The next breakthrough came from atomic physics: The invention of the atomic clock in 1949, followed by the first accurate cesium clock resonance measured in 1952. The development of cesium clocks over the next fifty years improved

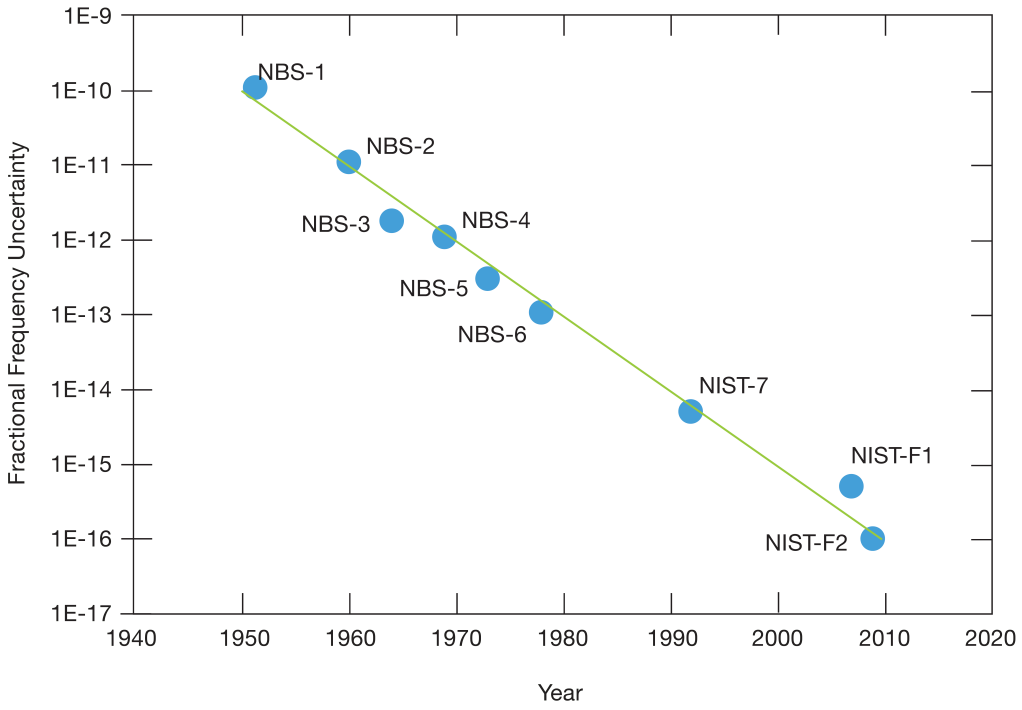

Figure 1.1: Clock development at the National Institute of Standards and Technology (NIST). Each datapoint shows either a newly developed atomic clock or a significant modification of an existing one. Adapted from [9].

their accuracy exponentially, becoming preciser by several orders of magnitude. For instance, the primary frequency standards developed at the National Institute of Standards and Technology (NIST) evolved from a relative accuracy of 1×10^{-11} in 1960 to 5×10^{-15} in 1998. The development of frequency standards at NIST is shown in Figure 1.1. [9] The progression of cesium clocks came to a halt as they reached the quantum-projection-noise at 1×10^{-16} [10, 11]. Since it scales reciprocal with the frequency of the interrogated clock transition [12], optical transitions offer greater stability than those in the microwave regime [13, 14]. A promising candidate, Al^+, possesses a suitable optical clock transition, but lacks the possibility of direct laser cooling and state detection, founding the development of so-called quantum logic spectroscopy [15]. Thereby a ground state-cooled

"logic" ion is co-trapped with the clock ion, cooling it sympathetically [15]. Transferring the quantum state from the clock to the logic ion, it can be used for state detection as well [15]. Optical clocks soon exceeded the capabilities of microwave clocks, keeping time with a precision of the order of 2×10^{-17}, an order of magnitude below the possibilities of cesium clocks [16]. Comparing different clock transitions of such precision allowed to set boundaries for the time variation of fundamental constants, e.g. proton-to-electron mass ratio $m_\mathrm{p}/m_\mathrm{e}$ or the fine-structure constant α [14, 16, 17].
To push these boundaries further, for the next generation of clocks the use of highly charged ions (HCIs) has been proposed, as they can possess narrow optical transitions and are less sensitive to external perturbations due to their strong internal field strengths [18, 19]. Additionally, some HCIs are among the most sensitive for possible effects caused by "new physics" and therefore of increased interest [19, 20]. As a proof of principle, boron-like Ar^{13+} has been examined by the means of quantum logic spectroscopy at the Physikalisch-Technische Bundesanstalt (PTB), improving the measurement of its M1 hyperfine transition by several orders of magnitude [21, 22]. As HCIs can not be generated in a trap suitable for such precision experiments, they are produced externally, extracted, injected via a beamline and re-trapped.

In this thesis, a setup to deliver HCIs for high precision traps is presented. An electron beam ion trap (EBIT) is used to generate the ions from neutrals, while the beamline transports them after extraction and prepares them for the injection and re-trapping.

Ch. 2 outlines the space charge effects on the electron beam and ionization processes present in an EBIT. It discusses the resulting evolution of charge states and makes considerations for extracting ions. The behavior of extracted ions in the presence of electric fields is analyzed and the bunching mechanism is explained shortly.

Ch. 3 gives an overview of the experimental setup built in the context of this work. The EBIT and its components are presented, as is the beamline composition. Special attention is given to the beam diagnostics, as all the measurements in this thesis were taken with it. The specifics of the vacuum system are given as well.

Ch. 4 consists of the measurements taken as part of this thesis. It reconstructs the process of starting to extract ions, identifying the charge states, maximizing and selecting the desired one, and optimizing the pre-cooling process.

Chapter 2

Theoretical basics

The term highly charged ions (HCIs) stands for ions that have higher charge states than typically achieved by most measures like chemical ionization, electric field ionization or photo-ionization. The production of highly charged ions evidently requires many subsequent ionization steps, so methods insensitive to the detailed electronic structure are used. There are two common methods: One uses impact ionization, with electron bombardment as in electron beam ion sources/traps or ions hitting stripper foils in storage rings. The other exploits the microwave resonance of the electrons with respect to an external magnetic field, as in electron cyclotron resonance ion sources. To produce HCIs in this work an electron beam ion trap (EBIT) was decided upon for reasons of feasibility and practicability. While this method is suitable to produce (and store) HCIs, it proved unsuitable for precision spectroscopy due to its strong magnetic field and high ion temperature, caused by its operational principle. Therefore a different trapping environment is needed to improve measurements. This can only be provided in an entirely different trap, demanding extraction, transportation and re-trapping of ions. The transfer of the ions is ensured by the beamline that is the centerpiece of this work: It guides ions using electrostatic ion optics, makes use of their time of flight separation for charge state selection and employs an electrodynamic bunching and deceleration mechanism to prepare them for re-trapping. The theoretical foundations, that underlie the work of principle of an EBIT and the corresponding beamline, are outlined in the following chapter.

2.1 Electron beam ion trap

EBITs yield HCIs by employing sequential electron impact ionization. An electron beam is accelerated from the negatively biased cathode, where the electrons are released, towards the collector, where they are restored, passing the trap center on the way. At the trap center injected neutral elements crossing the electron beam are ionized. The thus produced ions are now trapped by two electrostatic potentials: In the axial direction, an externally applied electric potential well prevents the ions to leave the trap, in the radial direction the negative space charge potential of the electron beam attracts the ions towards itself. This electrostatic trap configuration does not violate Earnshaw's theorem, which only applies in free space, as it includes the electron beam space charge as a source term. This way the ions cross the electron beam repeatedly and get ionized further. The high electron beam density needed for this process is achieved by compressing it by a strong magnetic field. Finally, the ions are extracted by inverting the axial potential well. The following sections will give the theoretical background essential for using an EBIT as a source for highly charged ions.

2.1.1 Electron beam energy

As the extracted ions are ionized at the trap center, the beam energy E_{beam} there is of interest. It consists of the elementary charge e as well as the applied voltage difference between trap center Φ_{trap} and cathode Φ_{cathode}. The total potential difference is furthermore modified by space charge effects at the trap center caused by the electron beam $\Phi_{\mathrm{SC_{e^-}}} < 0$ and the ion cloud $\Phi_{\mathrm{SC_{ion}}} > 0$. Additionally, E_{beam} needs to be corrected by the Fermi level $E_{\mathrm{Fermi}} > 0$ of the cathode surface to factor in the energy needed to extract the electron. This gives us

$$E_{\mathrm{beam}} = -e\left((\Phi_{\mathrm{trap}} + \Phi_{\mathrm{SC_{e^-}}} + \Phi_{\mathrm{SC_{ion}}}) - \Phi_{\mathrm{cathode}}\right) - E_{\mathrm{Fermi}}. \tag{2.1}$$

Generally, $|\Phi_{\mathrm{SC_{e^-}}}| > |\Phi_{\mathrm{SC_{ion}}}|$, therefore both, the Fermi level and space charge effects lower the electron beam energy, leading to a marginally lower beam energy than the simple estimation $E_{\mathrm{beam}} = e(U_{\mathrm{trap}} - U_{\mathrm{cathode}})$, that will be used for most of the following work.

2.1.2 Electronic processes

As discussed above, the ions trapped in an EBIT have an overlap with the electron beam, driving processes such as electron impact ionization, electronic excitation and electronic recombination. To achieve initial ionization, neutrals are injected into the EBIT in a way that the neutral beam crosses the electron beam. This additionally leads to an interaction of HCIs with the injected neutrals, that - as well as the interaction of HCIs with the background gas - can further cause charge exchange, the transfer of electrons to the involved HCI. Electronic recombination and charge exchange might, electronic excitation always does leave the HCI in an excited state, that decays either by the emission of a photon or by auto-ionization in the so-called Auger process. These transitions and their cross sections are going to be analyzed in the following sections.

Electron impact ionization (EII)

If the electron energy $E_\mathrm{e} \mathrel{\hat{=}} E_\mathrm{beam}$ exceeds the ionization energy E_i of an atom or ion, the interaction between this electron and the ion, respectively atom, can lead to ionization of the element A with the charge state q to the charge state $q+1$:

$$\mathrm{A^q} + e^-(E_\mathrm{e}) \rightarrow \mathrm{A^{q+1}} + e^-(E_\mathrm{e}^1) + e^-(E_\mathrm{e}^2), \quad E_\mathrm{e}^1 + E_\mathrm{e}^2 = E_\mathrm{e} - E_\mathrm{i} \geq 0 \tag{2.2}$$

with E_e^1 and E_e^2 giving the energies of the two free electrons after the process. The cross section $\sigma_{\mathrm{q}\rightarrow\mathrm{q+1}}^{\mathrm{EII}}$for this process depends mainly on E_beam and E_i, as discussed in [23]

$$\sigma_{\mathrm{q}\rightarrow\mathrm{q+1}}^{\mathrm{EII}} \approx \sum_{i=1}^{N} a_\mathrm{i} q_\mathrm{i} \frac{\ln\left(\mathrm{E_e}/\mathrm{E_i}\right)}{E_\mathrm{e} E_\mathrm{i}} \left(1 - b_\mathrm{i}\, exp\left[-c_\mathrm{i}\left(\frac{E_\mathrm{e}}{E_\mathrm{i}} - 1\right)\right]\right), \tag{2.3}$$

where each i represents a different sub-shell a removed electron can originate from. a_i, b_i and c_i are constants that have to be estimated, measured or calculated by theory. The general behavior of the cross section is plotted in Figure 2.1: A linear increase starting at $E_\mathrm{e} = E_\mathrm{i}$, the increase slowing down to reach a maximum towards $E_\mathrm{e} \approx 3E_\mathrm{i}$, followed by a decay for $E_\mathrm{e} \gg E_\mathrm{i}$ [24].

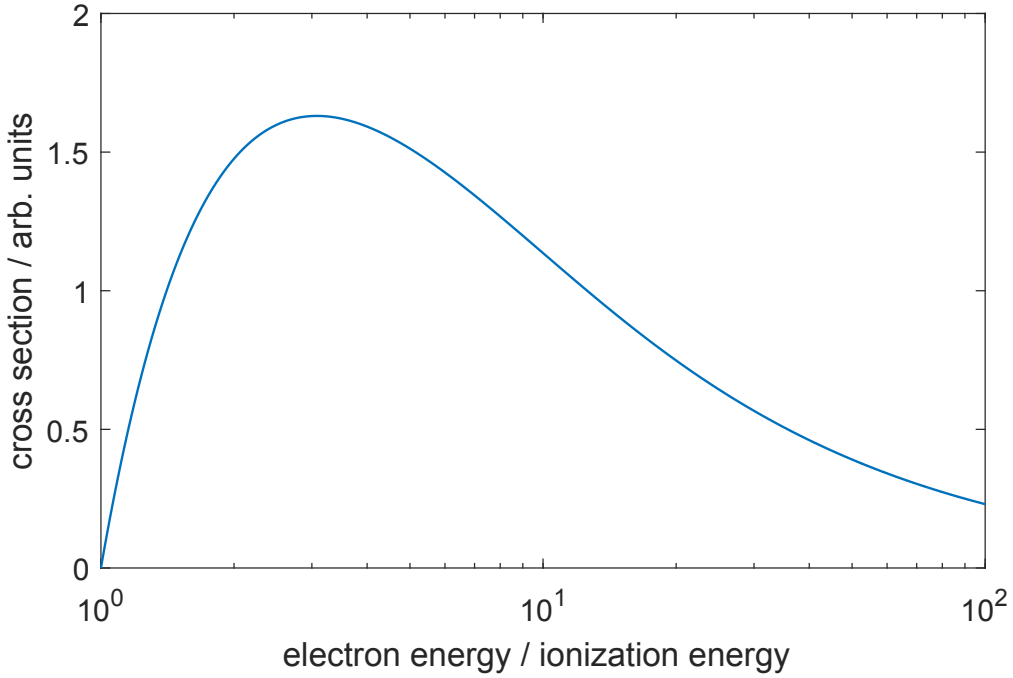

Figure 2.1: Behavior of the cross section of electron impact ionization for different electron energies. One clearly sees the initial increase to the maximum around 3 $E_\mathrm{e}/E_\mathrm{i}$, followed by a decline. Parameters chosen arbitrarily.

Electronic recombination

The interaction between ions and electrons in the trap can also lead to recombination of an ion with an electron. The excess energy $E_\mathrm{e} + E_\mathrm{i}$ is either transferred to a photon or, if the energy matches, resonantly to an electronic transition in the ion, transferring it into an excited state. The first process, involving the photon, is called radiative recombination (RR):

$$\mathrm{A}^\mathrm{q} + e^-(E_\mathrm{e}) \rightarrow \mathrm{A}^{\mathrm{q}-1} + \gamma(E_\gamma), \quad E_\gamma = E_\mathrm{e} + E_\mathrm{i}, \tag{2.4}$$

where γ is the photon and E_γ its energy. The cross section $\sigma^\mathrm{RR}_{\mathrm{q}\rightarrow\mathrm{q}-1}$ can be described semi-empirically as [25]:

$$\sigma^\mathrm{RR}_{\mathrm{q}\rightarrow\mathrm{q}-1} = \frac{8\pi}{3\sqrt{3}}\alpha\lambda\!\!\!^{-2}_\mathrm{C}\chi\ln\left(1+\frac{\chi}{2n^2_{0,\mathrm{eff}}}\right),\ \chi = 2Z^2_\mathrm{eff}\frac{R_\mathrm{y}}{E_\mathrm{e}}, \tag{2.5}$$

with the fine structure constant α, reduced Compton wavelength $\lambda\!\!\!^{-}_{\mathrm{C}}$, the effective nuclear charge $Z_{\mathrm{eff}} = 0.5(z+q)$, the Rydberg energy R_{y} and the effective principal quantum number $n_{0,\mathrm{eff}} = n_0 + 1 - w_0$, where w_0 gives the ratio between occupied and unoccupied states in n_0.
The second case, involving a second electron, looks the following:

$$\mathrm{A}^{\mathrm{q}} + e^-(E_{\mathrm{e}}) \rightarrow \left[\mathrm{A}^{\mathrm{q}-1}\right]^*, \quad \Delta E_{\mathrm{A}^{\mathrm{q}-1}} = E_{\mathrm{e}} + E_{\mathrm{i}}, \tag{2.6}$$

where $\Delta E_{\mathrm{A}^{\mathrm{q}-1}}$ is the excess energy of the excited electronic state of the resulting $A^{\mathrm{q}-1}$ ion. The cross section consideration is being omitted since this only occurs at resonant energies the EBIT was not operated at for the following work.

Electron impact excitation (EIE)

A free electron interacting with an ion can excite it without being captured:

$$\mathrm{A}^{\mathrm{q}} + e^-(E_{\mathrm{e}}) \rightarrow [\mathrm{A}^{\mathrm{q}}]^* + e^-(E'_{\mathrm{e}}), \quad \Delta E_{\mathrm{A}^{\mathrm{q}}} = \Delta E_{\mathrm{e}} = E_{\mathrm{e}} - E'_{\mathrm{e}}. \tag{2.7}$$

For i and j denoting different levels of the ion A, the cross section of the transition $i \rightarrow j$ can be approximated by the van Regemorter formula [26]

$$\sigma^{\mathrm{EIE}}_{i\rightarrow j} = \pi a_0^2 \frac{8\pi f_{\mathrm{ij}}}{\sqrt{3}} \frac{R_{\mathrm{y}}^2}{E_{\mathrm{ij}}^2} \frac{G(E_{\mathrm{e}}/E_{\mathrm{ij}})}{E_{\mathrm{e}}/E_{\mathrm{ij}}}, \tag{2.8}$$

where f_{ij} is the oscillator strength between both levels, E_{ij} the transition energy and $G(x)$ the effective Gaunt factor, a fitting function of order unity that can be approximated by [26]

$$G(x) = 0.349\ln(x) + 0.455x^{-1} + 0.0988. \tag{2.9}$$

Charge exchange (CHX)

The interaction between an atom B and a highly charged ion can cause a transfer of electrons from the atom to the HCI, emitting excess energy as an photon:

$$\mathrm{A}^{\mathrm{q}} + \mathrm{B} \rightarrow \mathrm{A}^{\mathrm{q}-1} + \mathrm{B}^+ + \gamma(E_\gamma), \quad E_\gamma = E_{\mathrm{i,A}^{\mathrm{q}-1}} - E_{\mathrm{i,B}}, \tag{2.10}$$

where $E_{\mathrm{i,A^{q-1}}}$ and $E_{\mathrm{i,B}}$ are the ionization energies of $\mathrm{A^{q-1}}$ and B respectively. If either of them end up in an excited state, E_γ is lowered by the excitation energy of $[\mathrm{A^{q-1}}]^*$ or $[\mathrm{B^+}]^*$. The cross section of this process is given by [27]:

$$\sigma^{\mathrm{CHX}}_{\mathrm{q\to q-1}} = \pi a_0^2 q^2 \frac{R_\mathrm{y}}{E_\mathrm{i,B}}^2, \tag{2.11}$$

with the Bohr radius a_0.

De-excitation

An excited ion or atom can decay in two pathways, either by radiation of a photon,

$$\left[\mathrm{A^{q-1}}\right]^* \to \mathrm{A^{q-1}} + \gamma(E_\gamma), \quad E_\gamma = \Delta E_{\mathrm{A^{q-1}}}, \tag{2.12}$$

or an electron, in a so called auto-ionization process, also called auger decay,

$$\left[\mathrm{A^{q-1}}\right]^* \to \mathrm{A^q} + e^-(E_\mathrm{e}), \quad E_\mathrm{e} = \Delta E_{\mathrm{A^{q-1}}}, \tag{2.13}$$

with a branching ratio depending on the internal electronic structure.

2.1.3 Charge state evolution

As for most applications the extraction of ions of a specific charge state is required, the processes that govern the charge state distribution of ions trapped in an EBIT are of further interest. In addition to the aforementioned processes, this distribution is affected by the influx of neutrals through the injection system (INF) as well as the escape rate (ESC) of the ions. The auger process is omitted for simplicity as branching ratios are unknown for most HCIs. This leads to the ion density evolution as described in [28]:

$$\dot{N}_\mathrm{q} = R^{\mathrm{EII}}_{\mathrm{q-1\to q}} - R^{\mathrm{EII}}_{\mathrm{q\to q+1}} + R^{\mathrm{RR}}_{\mathrm{q+1\to q}} - R^{\mathrm{RR}}_{\mathrm{q\to q-1}} + R^{\mathrm{CHX}}_{\mathrm{q+1\to q}} - R^{\mathrm{CHX}}_{\mathrm{q\to q-1}} + R^{\mathrm{INF}}_\mathrm{q} - R^{\mathrm{ESC}}_\mathrm{q}, \tag{2.14}$$

where N_q is the density of ions in the charge state q. The electron impact ionization rate is

$$R^{\mathrm{EII}}_{\mathrm{q\to q+1}} = \frac{J_\mathrm{e}}{e} N_\mathrm{q} \sigma^{\mathrm{EII}}_{\mathrm{q\to q+1}} f_{\mathrm{e,i}}, \tag{2.15}$$

where J_e is the electron beam density, $\sigma^{\mathrm{EII}}_{\mathrm{q}\to\mathrm{q}+1}$ is the cross section given in equation 2.3 and $f_{\mathrm{e,i}}$ is a factor that accounts for the overlap between electron beam and ion cloud. The radiative recombination rate is given by

$$R^{\mathrm{RR}}_{\mathrm{q}\to\mathrm{q}+1} = \frac{J_\mathrm{e}}{e} N_\mathrm{q} \sigma^{\mathrm{RR}}_{\mathrm{q}\to\mathrm{q}-1} f_{\mathrm{e,i}}, \tag{2.16}$$

with the cross section $\sigma^{\mathrm{RR}}_{\mathrm{q}\to\mathrm{q}-1}$ from equation 2.5. The charge exchange rate is estimated via

$$R^{\mathrm{CHX}}_{\mathrm{q}\to\mathrm{q}-1} = N_0(p_\mathrm{inj}) N_\mathrm{q} \sigma^{\mathrm{CHX}}_{\mathrm{q}\to\mathrm{q}-1} \bar{v}_q, \tag{2.17}$$

where N_0 gives the neutral gas density, mainly dependent on the injection pressure p_inj, $\sigma^{\mathrm{CHX}}_{\mathrm{q}\to\mathrm{q}-1}$ is the charge exchange cross section given in equation 2.11 and $\bar{v}_q$ is the mean ion velocity that, assuming thermal equilibrium and hence a Maxwellian distribution, can be calculated via

$$\bar{v}_q = \sqrt{\frac{8 k_\mathrm{B} T_\mathrm{i}}{\pi m_\mathrm{i}}}, \tag{2.18}$$

where m_i gives the mass of the ion, T_i the ion temperature and k_B the Boltzmann constant. The constant loading with neutrals and subsequent ionization leads to the source term

$$R^{\mathrm{INF}}_1 = \frac{J_\mathrm{e}}{e} N_0 \sigma^{\mathrm{EII}}_{0\to1} \quad \forall\, q = 1, \qquad R^{\mathrm{INF}}_\mathrm{q} = 0 \quad \forall\, q \neq 1. \tag{2.19}$$

Finally, the escape rate is given in [28]:

$$R^{\mathrm{ESC}}_\mathrm{q} = N_\mathrm{q} \nu_\mathrm{q} \left(\frac{\exp(-\omega_\mathrm{q})}{\omega_\mathrm{q}} - \sqrt{\omega_\mathrm{q}} [\mathrm{erf}(\omega_\mathrm{q}) - 1] \right), \tag{2.20}$$

where

$$\omega_\mathrm{q} = \frac{eqV}{k_\mathrm{B} T_\mathrm{ion}}, \tag{2.21}$$

with the trapping potential V and the total Coulomb collision rate of q-charged ions

$$\nu_\mathrm{q} = \sum_{\mathrm{k}\in\mathrm{Q}} \nu_{\mathrm{q,k}}\,,$$

with Q as set of all possible charge states and $\nu_{\mathrm{q,k}}$ given in [28], Equation (9) as ν_{ij}. These transition rates can be integrated to a time evolution of charge states, e. g. Figure 2.2.

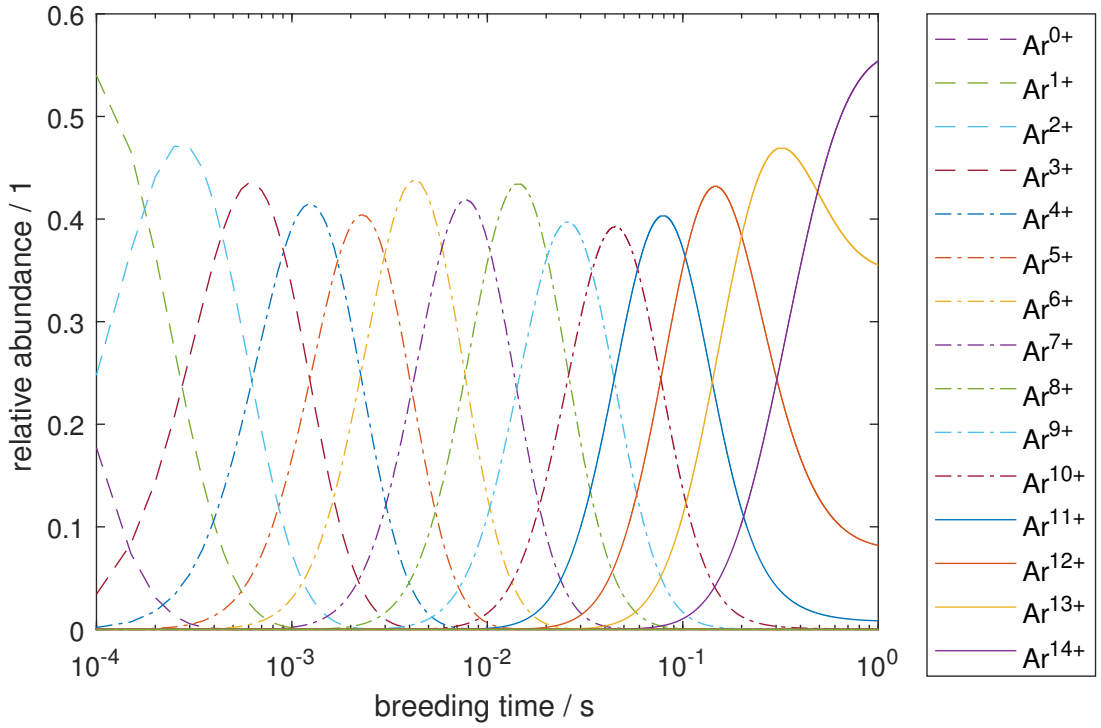

Figure 2.2: Simulation of the charge state evolution of argon. $E_e = 850\,\mathrm{eV}$, $J_e = 23\,\mathrm{A/cm^2}$, $f_{e,i} = 0.1$, $p_{bg} = 6.0 \times 10^{-10}\,\mathrm{mbar}$ were chosen as EBIT Parameters, corresponding to a electron beam current of $\sim 6.5\,\mathrm{mA}$. No continuous influx was used, but rather an initial population of 100 % neutral argon atoms. This also changes the dependence of N_0 for charge exchange to the residual gas pressure p_{bg}. The main charge state increases roughly exponentially with the breeding time. The sequential nature of the ionization process can be clearly seen. Simulation done by J. R. Crespo López-Urrutia.

2.1.4 Extraction

To extract ions from the EBIT, the axial confinement is reversed by lifting up the potential of the central trap electrode Φ_{trap} to a potential Φ_{kick}, which is more positive than the end cap potential Φ_{ec}. The ions are therefore accelerated axially out of the trap while being guided by the electron beam that still provides radial confinement. With the end cap potential being symmetric in most cases, the ions leave the trap in both directions, e.g. towards the extractor as well as the electron gun. The energy of the extracted ion E_{ion}

depends mainly on its charge state q and the acceleration potential Φ_{kick}. Additionally, one needs to consider the initial thermal energy distribution E_{T} as well as the fact that the ions can start leaving the trap once Φ_{trap} exceeds Φ_{ec}, even before it reaches Φ_{kick}. Furthermore, the space charge effects $\Phi_{\text{SC}} = \Phi_{\text{SC}_{\text{e}^-}} + \Phi_{\text{SC}_{\text{ion}}}$ discussed in section 2.1.1 play a role here as well. This results in the potentials and energy distribution:

$$E_{\text{ion}} = qe(\kappa\Phi_{\text{kick}} + \Phi_{\text{SC}}) + E_{\text{T}}, \tag{2.22}$$

where κ, with $1 \geq \kappa \geq \Phi_{\text{ec}}/\Phi_{\text{kick}}$ accounts for the fact that ions may leave before Φ_{kick} is reached. $|\Phi_{\text{SC}_{\text{e}^-}}| > |\Phi_{\text{SC}_{\text{ion}}}|$ still holds here, so space charge effects slightly decrease the energy of the extracted ions, but as above might be neglected for rough considerations. $\overline{E}_{\text{T}} = 0$ can be approximated, allowing the removal of this term for consideration of the energy of a whole ion bunch, where it is treated in the energy spread ΔE_{ion}, whose main cause it is. Unfortunately minor anisotropies - e.g. caused by preferences of ions with certain thermal velocities to leave the trap in a certain direction - are quite likely and can not be ruled out completely. In summary, for most cases, one can treat the energy of an ion bunch as

$$E_{\text{ion}} \approx qe\kappa\Phi_{\text{kick}},\ \Delta E_{\text{ion}} \approx \Delta E_{\text{T}}. \tag{2.23}$$

For an ion moving in ground potential, E_{ion} is equivalent to its kinetic energy E_{kin}.
Of further interest is the radial emittance ϵ of the resulting ion beam as, in combination with ΔE_{ion} and the bunch length $\Delta\sigma_{\text{z}}$, which treats the axial components, it describes the phase space volume the beam occupies. It is given in [29] as

$$\epsilon_{\text{r}} = \sigma_{\text{r}}\sqrt{\frac{E_{\text{T}}}{3qe\kappa\Phi_{\text{kick}}}}, \tag{2.24}$$

where σ_{r} stands for the average spacial spread in the radial direction. Unfortunately, that results in limited control over the phase space volume occupied by the extracted ions, as both the temperature and the spatial spread can only be influenced to a small degree. The velocity of the extracted ion of the mass m can further be estimated as

$$v_{\text{ion}} = \sqrt{\frac{2E_{\text{ion}}}{m}} = \sqrt{\frac{2qe\kappa\Phi_{\text{kick}}}{m}}. \tag{2.25}$$

2.2 Beamline

Extracted ions repel each other due to their charge, defocusing the ion beam along the way of transportation, even if it is perfectly collimated initially. Aside from that, a variety of inaccuracies - the relative positioning of vacuum chambers, the actual assembly of electrodes inside the chambers, roughness of electrode surfaces, asymmetries in the magnetic field of the EBIT, instabilities of power supplies e. g. - additionally lead to diversion and distortion of the ion beam. As a result, ion optics are implemented into the beamline to correct such effects, increasing the ion transport efficiency. Furthermore, a 90°-deflector is required for optical access along the ion beam axis. The general working principle of ion optics and their influence on the time of flight are explained hereafter.
Apart from assuring efficient transport of ions the beamline also prepares them for re-trapping. This is obtained on-line by employing a fast switching in-trap lift with a linear increasing electric potential. A rough assessment of its pre-cooling mechanism is outlined at the end of this chapter.

2.2.1 Ion optics

The ion optics used for this experiment are all based solely on electrostatic fields with the potential ϕ. They exert a force

$$\vec{F} = qe\vec{E} = qe\vec{\nabla}\phi \tag{2.26}$$

on each passing ion. The acceleration $\vec{a} = \vec{F}/m$ calculated from that and the initial ion velocity given in equation 2.25 lead to the equation of motion

$$\vec{r}(t) = \frac{\vec{a}}{2}t^2 + \vec{v}_0 t + \vec{r}_0 = \frac{\vec{\nabla}\phi}{2}\frac{qe}{m}t^2 + \sqrt{2\kappa\Phi_{\text{kick}}}\sqrt{\frac{qe}{m}}t\vec{e}_z + \vec{r}_0, \tag{2.27}$$

where $\vec{e}_z$ denotes the direction on the beam axis. Reparameterization of t with

$$\tau = \sqrt{\frac{qe}{m}}t \tag{2.28}$$

leads to

$$\vec{r}(\tau) = \frac{\vec{\nabla}\phi}{2}\tau^2 + \sqrt{2\kappa\Phi_{\text{kick}}}\vec{e}_z\tau, \tag{2.29}$$

independent of qe/m, showing that the path through the ion optical elements does not depend on the ions charge or mass. Different ions (A, B) arrive at any given point $\vec{r}$ at the same τ, meaning their time of arrival correlates via

$$\sqrt{\frac{q_A e}{m_A}}t_A = \tau_A = \tau_B = \sqrt{\frac{q_B e}{m_B}}t_B, \tag{2.30}$$

$$t_A = \sqrt{\frac{q_B m_A}{q_A m_B}}t_B. \tag{2.31}$$

Considering highly charged ions of the same element, with the same mass m, but different charge states q, we can easily calculate the time t_q from the time t_1 of the slowest ion of charge state $q = 1$ with

$$t_q = \frac{t_1}{\sqrt{q}}. \tag{2.32}$$

2.2.2 Bunching mechanism

To slow down the ions before entering the second trap, the beamline is equipped with an electrodynamic in-trap lift, with a linearly increasing potential along the beam axis z [30]. The potential is approximated by

$$\Phi(t, z) = \Theta(t_{\text{s}} - t)\left[\Phi_{\text{avg}} + \Phi_{\text{diff}}\frac{z - z0}{d_{\text{z}}}\right], \tag{2.33}$$

where $\Theta(x)$ is the unit step function, t_s the switching time, Φ_{avg} the average of potential as well as Φ_{diff} the difference in potential of both electrodes, z_0 the center between both electrodes and d_z the distance between them.
The ions reach the potential, are decelerated according to their position z, at t_s the potential decreases almost instantaneously, reducing the ion energy by

$$\Delta E(z) = qe\Phi(t < t_{\text{s}}, z) = qe\left[\Phi_{\text{avg}} + \Phi_{\text{diff}}\frac{z - z0}{d_{\text{z}}}\right], \tag{2.34}$$

depending on their position z at t_s. This can be divided into a position independent

$$\Delta E_{\mathrm{ind}} = qe\Phi_{\mathrm{avg}} \tag{2.35}$$

and dependent part

$$\Delta E_{\mathrm{dep}}(z) = qe\Phi_{\mathrm{diff}}\frac{z - z0}{d_{\mathrm{z}}}. \tag{2.36}$$

Since $z_{\mathrm{ion}}(t) = v_{\mathrm{ion}}t$ holds and t_s can be chosen accordingly to let the centroid of the ion bunch arrive at z_0, $z_{\mathrm{ion}}(t_s) = z_0$ and $\Delta E_{\mathrm{dep}}(z_{\mathrm{ion}}) = 0$. Using equation 2.25 in addition, the location of a ion with a slightly different energy, $E'_{\mathrm{ion}} = E_{\mathrm{ion}} \pm \delta E$, is considered:

$$z(t_s)' = v'_{\mathrm{ion}}t_s = \sqrt{\frac{2E_{\mathrm{ion}} \pm \delta E}{m}}t_s \approx \sqrt{\frac{2E_{\mathrm{ion}}}{m}}t_s \pm \sqrt{\frac{\delta E}{m}}t_s = z_0 \pm \sqrt{\frac{\delta E}{m}}t_s, \tag{2.37}$$

using the 1st order Taylor expansion$\sqrt{x \pm 1} \approx 1 \pm x/2$ and assuming $z'(0) = z(0)$, which roughly holds with $t = 0$ as point in time for the extraction from the EBIT. While $\Delta E'_{\mathrm{ind}}$ stays the same, combining equation 2.37 and equation 2.36 gives

$$\Delta E'_{\mathrm{dep}}(z'(t_s)) = \pm qe\Phi_{\mathrm{diff}}\sqrt{\frac{\delta E}{m}}\frac{t_s}{d_{\mathrm{z}}}. \tag{2.38}$$

Hence, the HCIs with a lower (higher) energy compared to the mean ion bunch loose less (more) energy in the slow down process, reducing the overall ion energy spread. While d_z and t_s are fixed by the experimental layout, Φ_{diff} can be tuned to minimize the energy spread. For further considerations of that process, including simulations, refer to [31].

Chapter 3

Experimental setup

The experiment assembled for this work is conceptually separated into two main parts: the electron beam ion trap (EBIT) and the beamline. This is reflected in the actual experimental setup that will be discussed in the following chapter. In the EBIT chamber, neutral atoms are injected, ionized and charge bred to extract highly charged ion (HCI). For that reason it houses the injection system, the electron gun and collector, to produce an electron beam, as well as the drift tubes, to trap the ions, and is surrounded by the magnet system needed for electron beam compression. The beamline accommodates different electrostatic ion optics, the pulsed drift tube (PDT) and two detectors for beam analysis, assuring efficient ion transport and enabling the preparation for precooling. The diagnostic means are in the form of microchannel plate (MCP) detectors to perform time-of-flight and energy measurements. A schematic overview of the beamline and the cross section of the CAD model are given in Figure 3.1. A photograph of it is seen in Figure 3.2. At the end of the beamline, beyond the last MCP, a DN60CF gate valve is mounted to connect the ion source to a trap receiving the ions, e. g. the new superconducting quadrupole ion trap developed at this institute [32, 33].

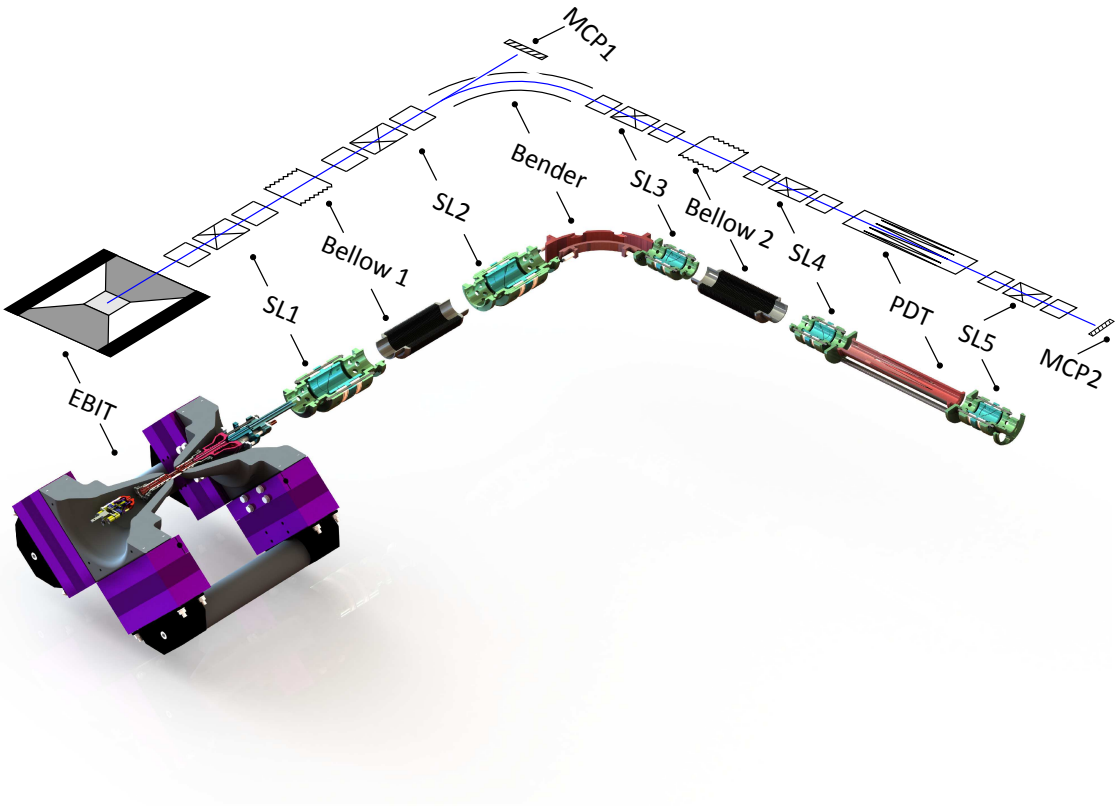

Figure 3.1: Intersection of the CAD model and schematics of the experimental setup. The principal ion path in the schematics is shown in blue. The produced HCIs are extracted from the EBIT towards MCP 1. SL 1 and SL 2 are used to steer and focus the ion beam through the hole in the bender onto MCP 1, with the bender on ground potential. The bifurcation depicted at the entrance of the bender represents the two possibilities to guide the ion beam, depending on the usage of the bender. Applying voltages on the bender enables the other ion path towards MCP 2. Here SL 3-5 are used for steering and focusing, while SL 3 additionally functions as kicker electrodes for charge state selection. The PDTs serve as a deceleration, bunching and pre-cooling unit. The second MCP facilitates energy measurements of an ion bunch featuring a retarding field analyzer in the form of two metal grids. It is further mounted on a retractable manipulator, allowing the possibility to transport the ions further into the Paul trap. A photograph of the whole setup can be seen in Figure 3.2

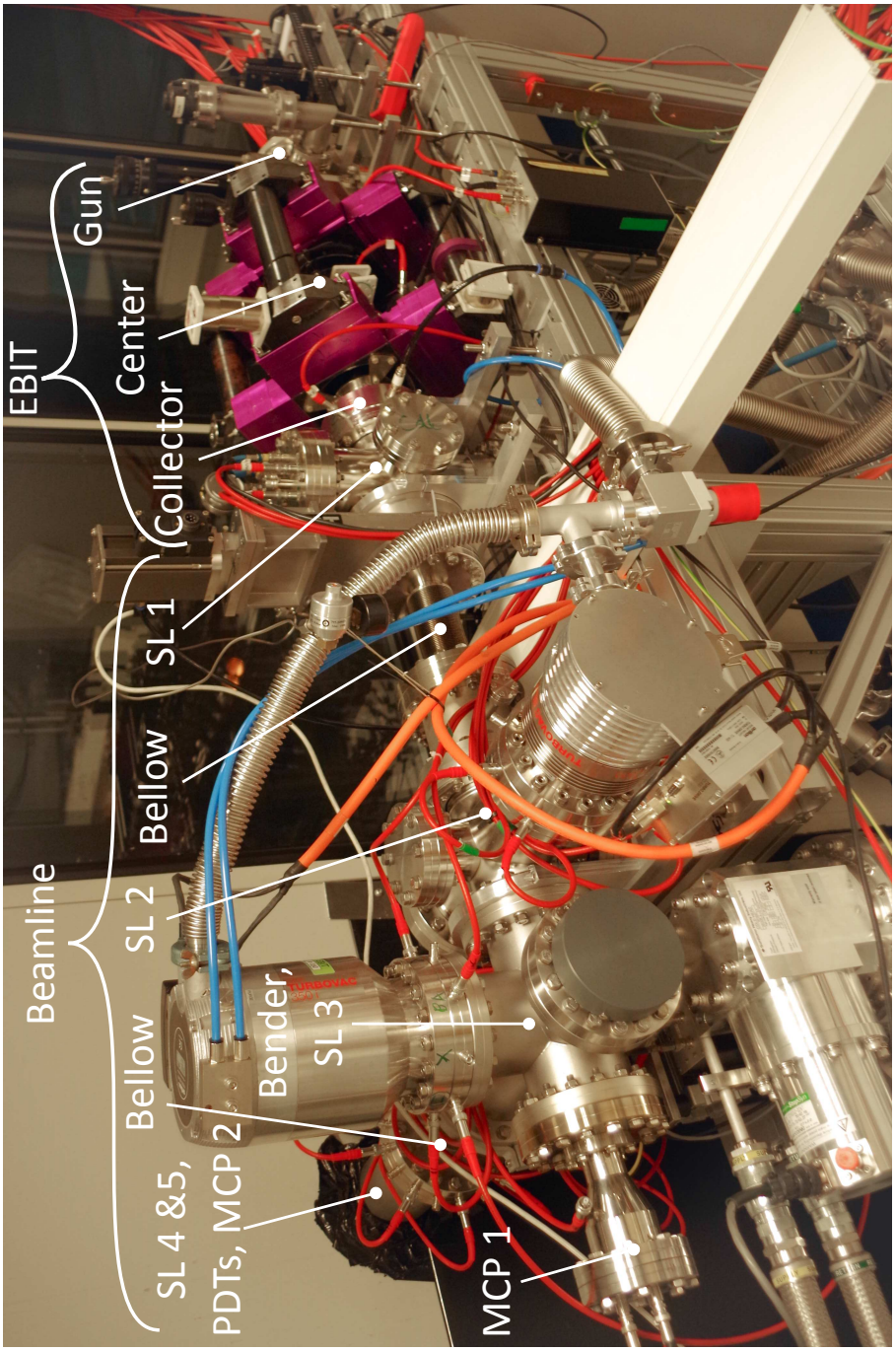

Figure 3.2: Photograph of the experimental setup, depicting the vacuum chambers for the elements outlined in Figure 3.1. The last part of the beamline, housing the PDTs, SL 4&5 and MCP 2, is located partially in a second laboratory.

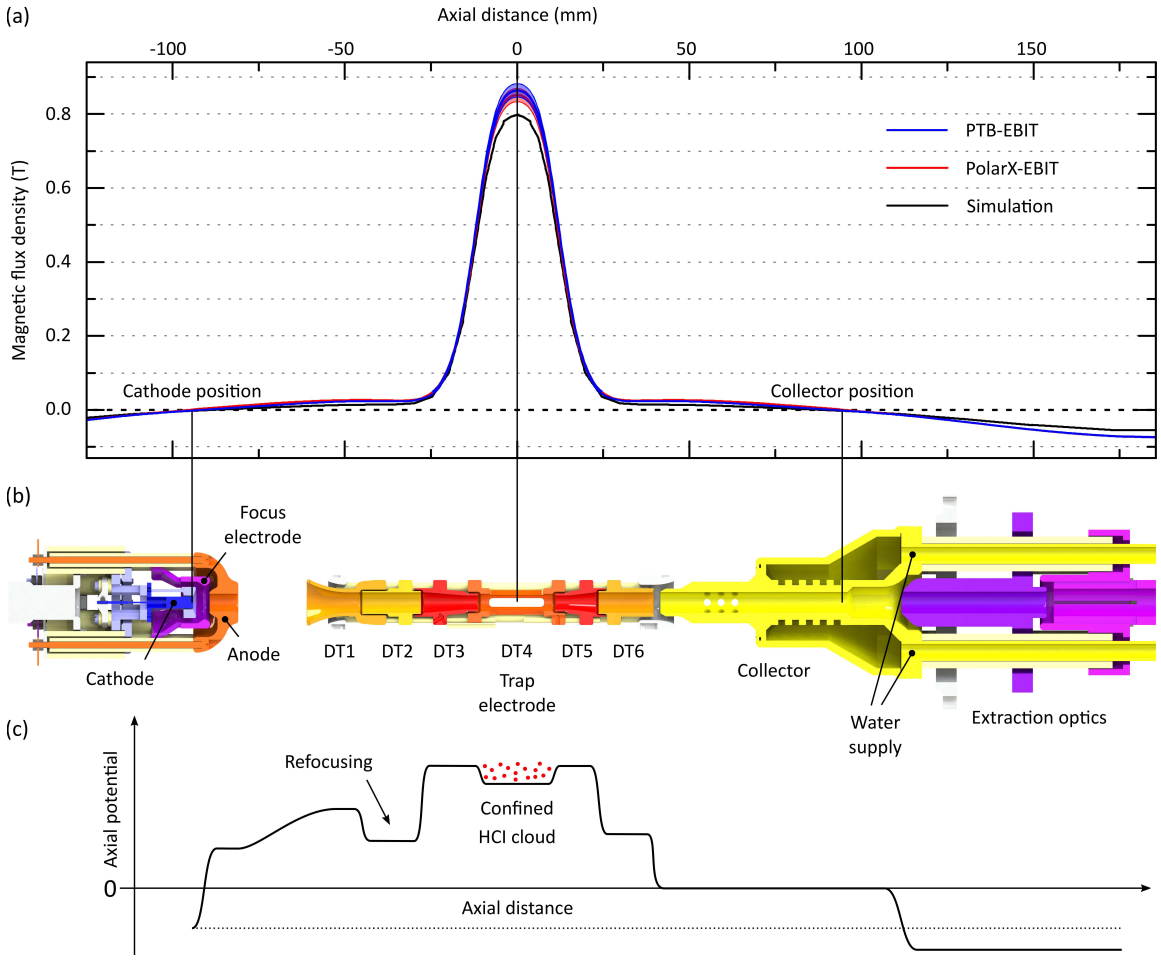

Figure 3.3: (a) Magnetic field landscape of the EBIT along the electron beam axis. The red and blue lines are measurements of two EBITs of the same type as the one used here, while the black line represents simulated values. The gun and collector are located on the zero-crossing, while the trap center is at maximum field strength, leading to optimal electron beam (de-)compression. (b) Cross section of the interior of the EBIT. From left to right: Gun with cathode, focus and anode electrodes; trap electrodes, also known as drift tubes, DTs 1-6; collector including extraction optics. Voltages applied to these electrodes form the electrostatic potential landscape plotted below. (c) Axial electrostatic potential landscape on the electron beam axis. The potential of the cathode is indicated by a dotted line, as it is the reference potential for the electrons. DTs 3-5 form the potential for ion trapping, with trapped ions depicted in red. Figure taken from [34].

3.1 Electron beam ion trap

A Heidelberg compact electron beam ion trap (EBIT) is used as dedicated device to supply HCIs. Its general working principle was explained in chapter 2. An overview of its internal components, as well as the magnetic and electrostatic potential landscape, is given in Figure 3.3. A short overview follows here, but a more detailed description can be found in [34]. Operating at room temperature, abolishing superconducting magnet coils used before, they have proven to be more cost-effective and small but powerful devices. Instead, their magnetic field, shown as up to 0.86 T, is produced by an array of permanent magnets, as described in Section 3.1.1 [34]. The electron beam is produced in an electron gun that is described in Section 3.1.2. The setup of the trap center, creating the axial potential well, is shown in Section 3.1.3. The collector setup, to stop the electron beam, is treated in Section 3.1.4. Currents up to 80 mA and energies up to 10 keV have been demonstrated, with ion beam currents extracted through the collector reaching 100 pA [34]. The trap can be accessed through four DN40CF ports on the sides of the cubical trap chamber. To load neutral atoms into the EBIT for charge breeding, a gas injection system is used on one of these ports, see Section 3.1.5.

3.1.1 Magnetic structure

A total of 72 cylindrical magnets, arranged in eight arrays of 3×3, positioned in a four-fold symmetry around the trap axis, are utilized to compress the electron beam. The dimension of each NdFeB magnet is 45 mm in diameter and 30 mm in height and magnetized along the cylinder axis. They are kept in place by aluminum cartridges, holding three magnets each. Yokes of soft iron shape the magnetic field as depicted in Figure 3.4 Four rods connect the outer side of the magnetic arrays around the trap, closing the magnetic flux. Two hollow cones form the poles around the trap, distributing the magnetic field nearly symmetrical into the trap center. Inside the cones is a bi-conical vacuum chamber containing the electron gun and the collector on opposite sides. The trap center is located inside a cube-shaped part between the cones, where the yoke has a 19 mm long, 19 mm diameter magnetic gap. The structure was simulated and designed to provide a high flux density inside the trap center as well as zero field at the cathode position to ensure a high beam compression, while the collector is positioned around the second zero-field node,

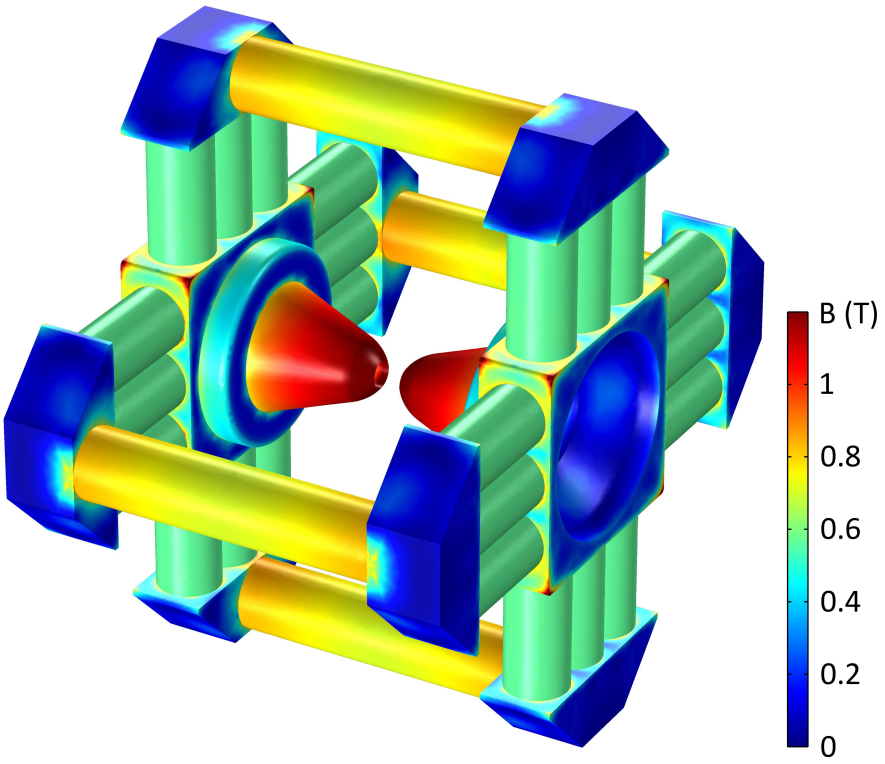

Figure 3.4: Simulated magnetic structure of the EBIT. The permanent magnets, produce a field of roughly 0.55 T each, appearing in teal. Soft-iron yokes guide and nearly close the magnetic flux, except for the trap center between the two cones, where it reaches a maximum along the trap axis of 0.86 T. Figure taken from [34].

allowing the electron beam to decompress. The magnetic flux on the beam axis can be seen in Figure 3.3(a).

3.1.2 Electron gun

To sustain a stable, milliampere strong electron beam, a thermionic dispenser cathode, consisting of a barium-permeated tungsten matrix, is used. In this type of cathode, a depletion of barium is prevented by a huge reservoir in the matrix that subsequently re-activates the surface. Poisoning of the cathode induced by ion contamination is prevented by limiting the materials in its vicinity to molybdenum, alumina ceramics and oxygen-free copper (requiring a slight separation). The cathode is held in place in an on-axis Pierce-

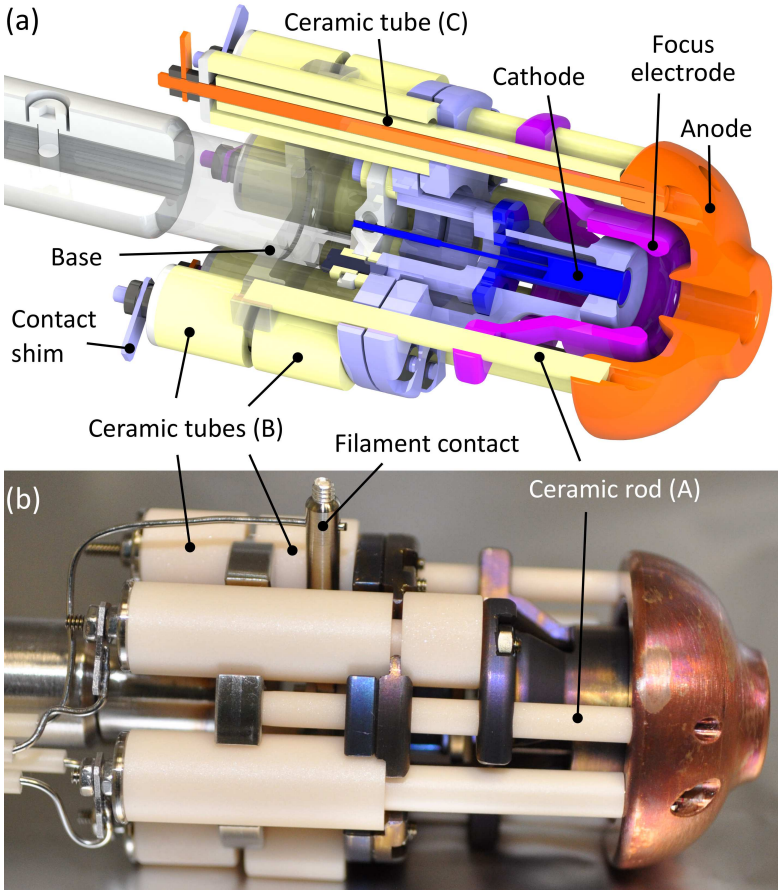

Figure 3.5: Cross section of the CAD model (a) and photograph (b) of the Pierce-type electron gun design used in the EBIT. Figure taken from [34].

type electron gun design, as can be seen in Figure 3.5. The gun consists of a cathode and a focus, both molybdenum, and an anode, copper, electrode, featuring rotational symmetric inner surfaces, as well as a stainless steel mounting plate on the back. Featuring an open design to ensure ultra-high vacuum on the cathode surface, they are held in place by alumina ceramics tubes and cylinders, clamped together by molybdenum threaded rods and stainless steel screws which also act as electrical wiring. The barium surface of the cathode is shielded from all stainless steel parts by either electrodes or ceramic tubes. The gun can be moved in all directions using manipulators to optimize the electron beam conditions, e. g. zero magnetic field, as discussed in Section 3.1.1, or its position relative to the drift tubes. The resistance heated barium cathode sets free electrons that are accelerated

by a negative voltage on the cathode - relative to the grounded collector, described in Section 3.1.3 - to produce an electron beam. The resulting current can best be controlled and stabilized employing the focus electrode. With a suitable anode voltage, an efficient transmission into the positively biased drift tubes, further discussed in Section 3.1.3, is ensured.

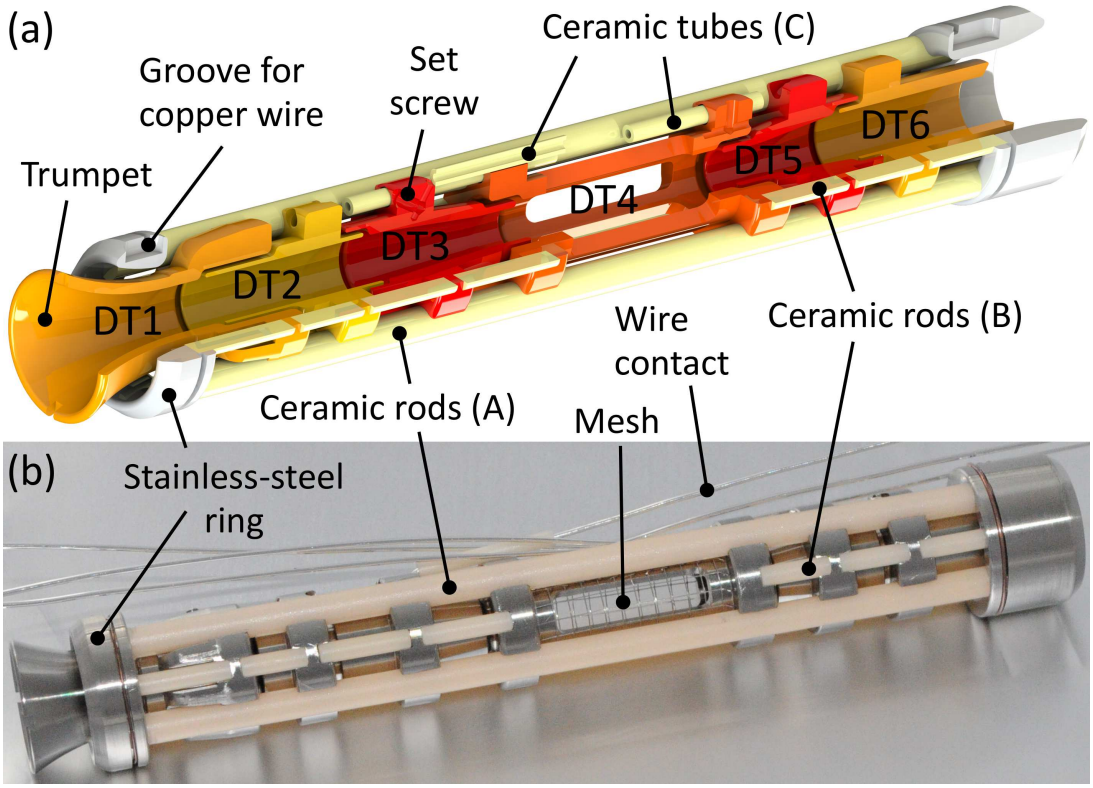

Figure 3.6: Cross section of the CAD model (a) and photograph (b) of the drift tube assembly employed in the EBIT. All electrodes remain rotationally symmetric, with occasionally reducing radii towards the trap center, labeled DT 4. In (b) the mesh around DT 4 is visible, as well as the not yet insulated electrical contact - with ceramic tubes (C) missing. Where (a) exhibits a groove for a copper wire - to hold the ceramic rods (A) in place - the fitted wires can be seen in (b). The small rods (B) are held in place by the groove of the electrodes. Figure taken from [34].

3.1.3 Drift tubes

While the radial confinement is ensured by the negative space charge potential of the electron beam, the axial confinement is achieved by cylindrical, positively biased electrodes, the so-called drift tubes (DTs)(seen in Figure 3.3). The central one, DT 4, is set to a lower positive potential than the surrounding DTs 3 and 5, creating an axial potential well. This voltage, the depth of the potential well, is often referred to as trap depth. For ion extraction the DT 4 voltage is increased for a short time, typically ~µs, inverting the trap and expelling the ions. The central drift tube is designed to have four access windows, which are provided with an etched grating to reduce reach-through from the ground potential of the surrounding vacuum chamber. They can be used for the gas injection system or different types of photon detectors e.g. an X-ray detector etc. The remaining drift tubes are tuned to optimize the electron beam transmission trough the EBIT, using mostly DT 1 and DT 2, as they can refocus the beam towards the trap center, and increase the extraction efficiency, using mostly DT 6. The electrodes are made from a titanium compound, held in position by alumina ceramics and secured by two flexible copper wires, as can be seen in Figure 3.6.

3.1.4 Collector

The collector consists of three different electrodes: The collector electrode, the 1st extraction tube and the 2nd extraction tube. The setup can be seen in Figure 3.7. Leaving the drift tubes, the electron beam reaches the collector electrode, which is on ground potential, and is slowed down. Additionally, the magnetic field landscape - as seen in Figure 3.3 - causes the electron beam to decompress and hit the wall. It is followed by the first extractor tube on a more negative potential than the cathode to guarantee the electron beam can not leave the EBIT. The second extractor electrode can be tuned more freely. Both extractor electrodes are used to maximize the extracted ion yield. All electrodes in the collector are made from copper and stacked together using alumina ceramics for separation. To prevent heating by the electron beam, the collector electrode is water-cooled using insulated fluid feed-troughs which also allow a measurement of the current on the collector to determine the electron beam transmission.

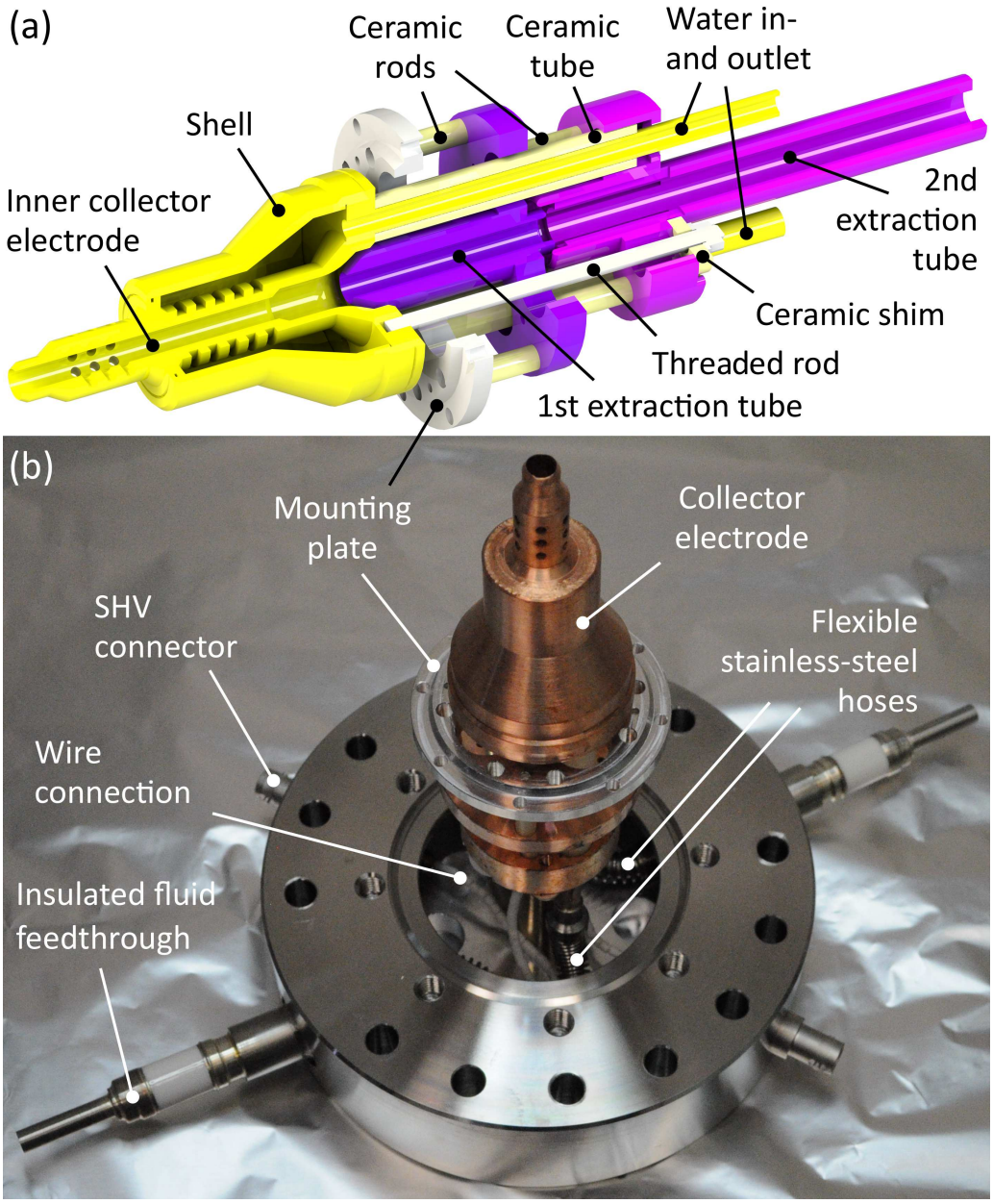

Figure 3.7: Cross section of the CAD model (a) and photograph (b) of the collector and extraction electrodes used in the EBIT. The photograph also includes parts of the vacuum chamber with fluid feedthroughs connected via stainless-steel hoses to cool the collector electrode. Figure adapted from [34].

3.1.5 Injection system

In order to load neutrals into the EBIT, it employs a single-stage gas injection system. Its vacuum chamber, evacuated by a turbo-molecular pump, is filled with the desired gas from a reservoir, ~ 1 bar, via a needle valve to regulate the injection pressure, typically between 5.0×10^{-9} mbar to 5.0×10^{-7} mbar. The connection to the trap center features an aperture to ensure the injected atom beam crosses the electron beam and is ionized. The reservoir is essentially a T-piece with the needle valve on one side and a DN25KF flange and a 6 mm rubber hose connection, respectively, on the other sides. Both connections can be closed off via a rotary valve. This not only offers flexibility on how to connect different injection gases, but it also enables to flush the resolver by connecting it to a membrane pump and an injection gas simultaneously, therefore reducing residual gas and air contamination.

3.2 Beamline

The beamline is designed to transport the ions efficiently from the EBIT to a colder trapping environment, e.g. a Paul trap and also exhibits a mechanism to perform phase space cooling along the way. It consists of five Sikler lenses (Section 3.2.1) for focusing and steering, one self-focusing electrostatic bender (Section 3.2.2) to allow optical access along the beam axis to the trap it is connected to, the pulsed drift tube (Section 3.2.3) for precooling and bunching as well as detectors (3.3) for beam analysis. The arrangement of these components can be seen in Figure 3.1. The beamline is an advancement of the beamline designed by L. Schmöger [30, 31, 35] and has been developed by P. Micke for a similar experiment at the Physikalisch-Technische Bundesanstalt Braunschweig in a collaboration with the Max-Planck-Institut für Kernphysik [21]. The following sections describe the beamline elements in more detail.

3.2.1 Sikler lens

The design of a Sikler lens (SL) is based on that of an einzel lens with the central lens split into four parts by two orthogonal cuts 45° askew from its symmetry axis. The grounded front and back electrodes are kept whole, leading to the design depicted in Figure 3.8. The electrodes are referred to by their position from the reference frame of the ion beam as Top-Left(TL), Top-Right(TR), Bottom-Left(BL) and Bottom-Right(BR). The resulting four degrees of freedom can be used as ion optics in the following way:

- Focus: Biasing all four electrodes with a certain voltage essentially uses the SL as an einzel lens, affecting the focus of the ion beam

- Steering: Grouping two adjacent electrodes together, e.g. BL+BR and TL+TR, and superimposing the focus voltage with a voltage between those groups, enables steering. The ions are steered in the direction of the normal vector of the resulting separation plane, in this case, up or down, depending on the sign of the voltage. The other possibility of grouping adjacent electrodes - BL+TL, BR+TR - results in left-right steering and can be overlayed as it is linearly independent. This allows steering in all directions, with up-down and left-right being the principal steering axis.

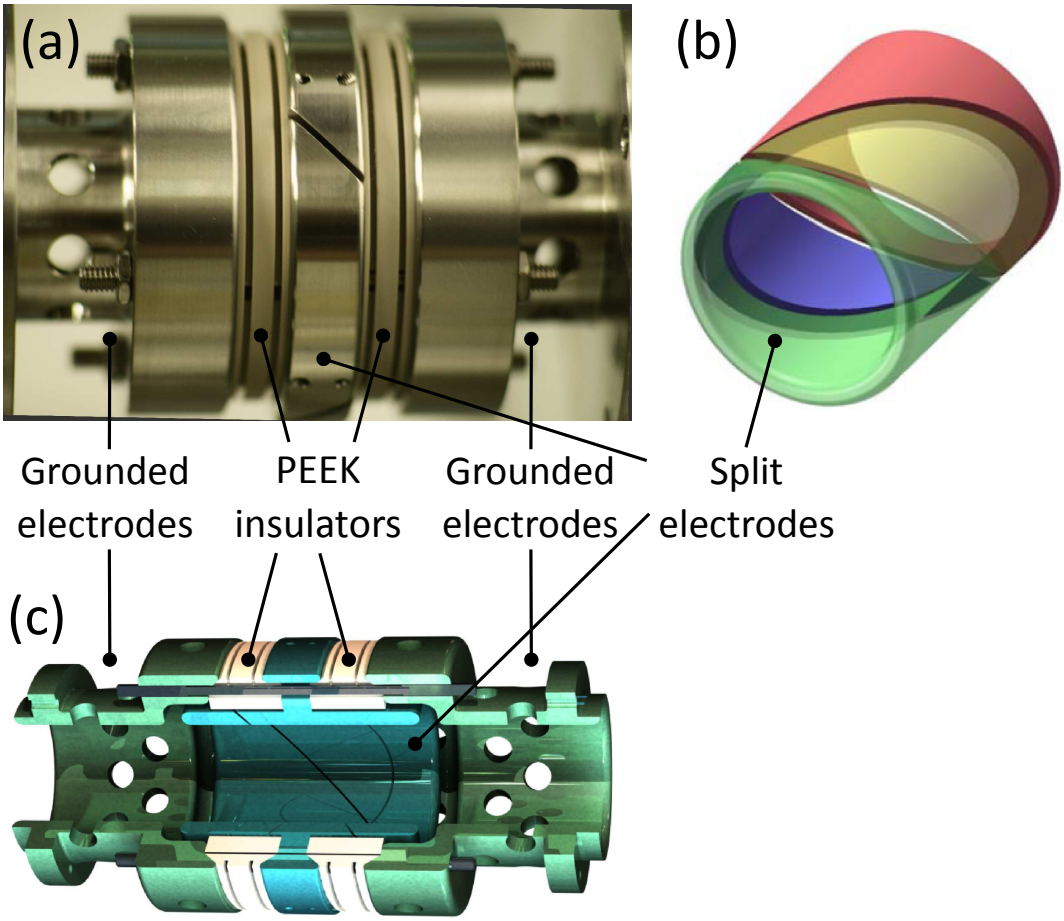

Figure 3.8: Photograph (a), schematic (b) and cross section of the CAD model of a Sikler lens (c). Part of the segmentation of the central electrode can be seen in the upper center of (a). On the resulting electrode-sections in (a), one can see a plain bore for electrical connection and threaded bore for the setscrew. (b) clarifies the electrode division: Top-Left(TL), Top-Right(TR), Bottom-Left(BL), Bottom-Right(BR).

- Astigmatism: Grouping together opposite electrodes, BL+TR and TL+BR, allows control over the astigmatism of the ion beam, by offsetting their voltage as above for steering. Note that only one of the two orthogonal astigmatism components can be corrected per SL, depending on their electrode positions, with the astigmatism axis turned 45° to the principal steering axis. To have control over both astigmatism components, some SLs are rotated 45° around their cylinder axis relative to the others.

The steering properties of an SL can also be used to select a distinct time window of an extraction cycle, e.g. a certain charge state, by changing the steering between 'towards next element' and 'vacuum chamber' respectively, using a fast high voltage switch. The four central electrodes are centered by two conical polyether ether ketone (PEEK) rings, which also insulates them from the grounded electrodes, tightened by four threaded rods. An equidistant rotational setup (and therefore sufficient electrical insulation between the central electrodes themselves) is ensured by inserting spacing shims before tightening the rods and removing them afterward. To mount the whole unit into the vacuum chamber, the grounded outer electrodes are connected to centering apertures or other experimental components, depending on their position.

3.2.2 Electrostatic bender

The 90°-deflector consists of two hollow cylinder segments of different radii and heights, with the respective measures chosen in a way to enable a double-focusing effect, that is not only in the plane of deflection but also orthogonal to it, as described in [36]. Access straight through the bender - to extract ions on MCP 1 or to feed a laser through the beamline, in direction of MCP 2 - is ensured by two bores in the outer electrode, whose projections are circular on their respective x-y-plane. To allow further control over the ion beam after the deflection, SL 3 is mounted directly behind the exit of the bender using ceramic spacers. It is attached by three centering apertures - one at the entrance, one opposite to it, insulated from the electrodes by ceramic spacers, and another to the grounded part of SL 3. For electrical connection, Kapton insulated copper wires are attached to the electrodes using bores and set screws. The setup is shown in Figure 3.9.

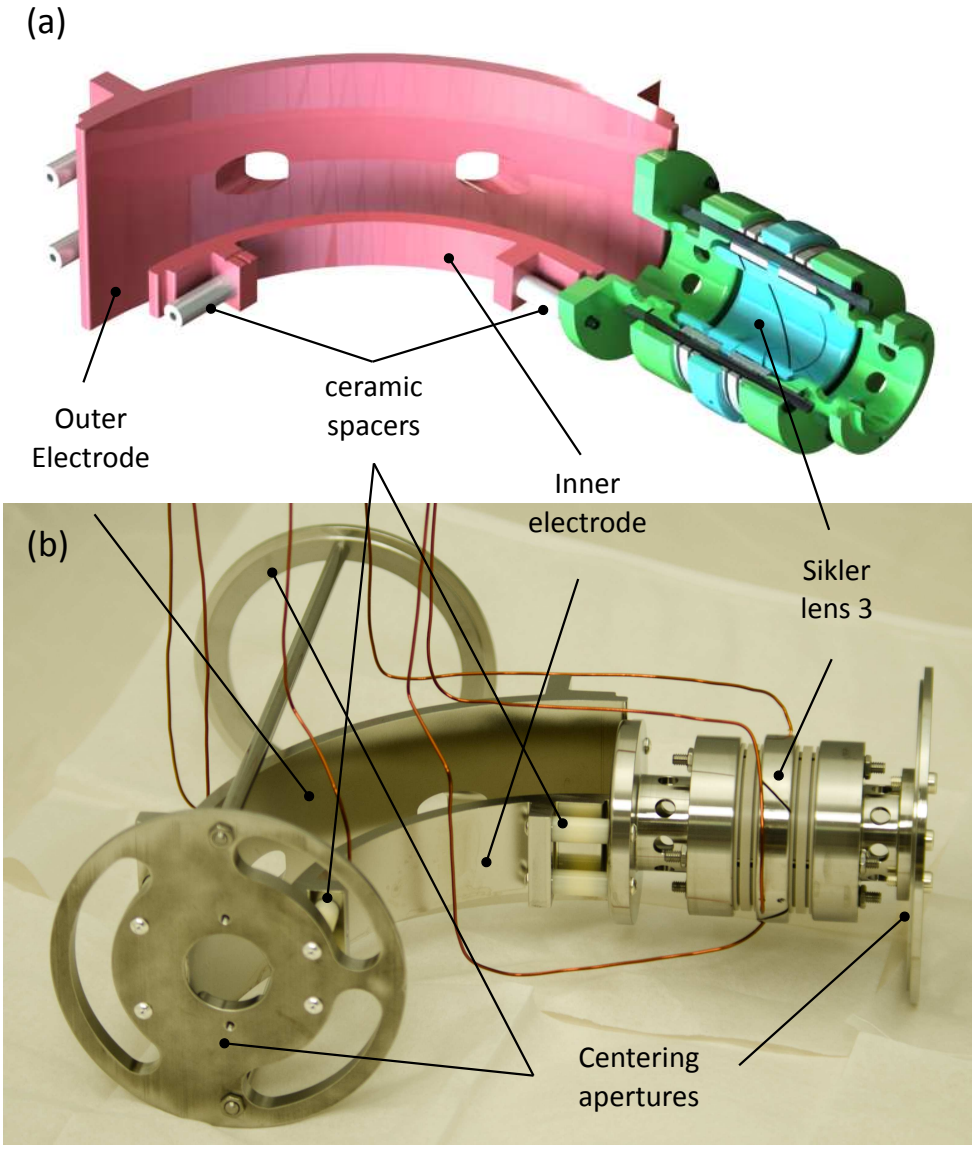

Figure 3.9: Cross section of the CAD model (a) and photograph (b) of the electrostatic Deflector on the left and SL 3 on the right. (b) shows centering apertures on the front, back and to the right that are used to mount the unit, insulated with ceramic spacers, into its vacuum chamber, as well as electrical connection guided to the top, made from UHV-suitable Kapton-insulated copper wires. One sees the difference in height between both cylinder segments that provide the self-focusing effect.

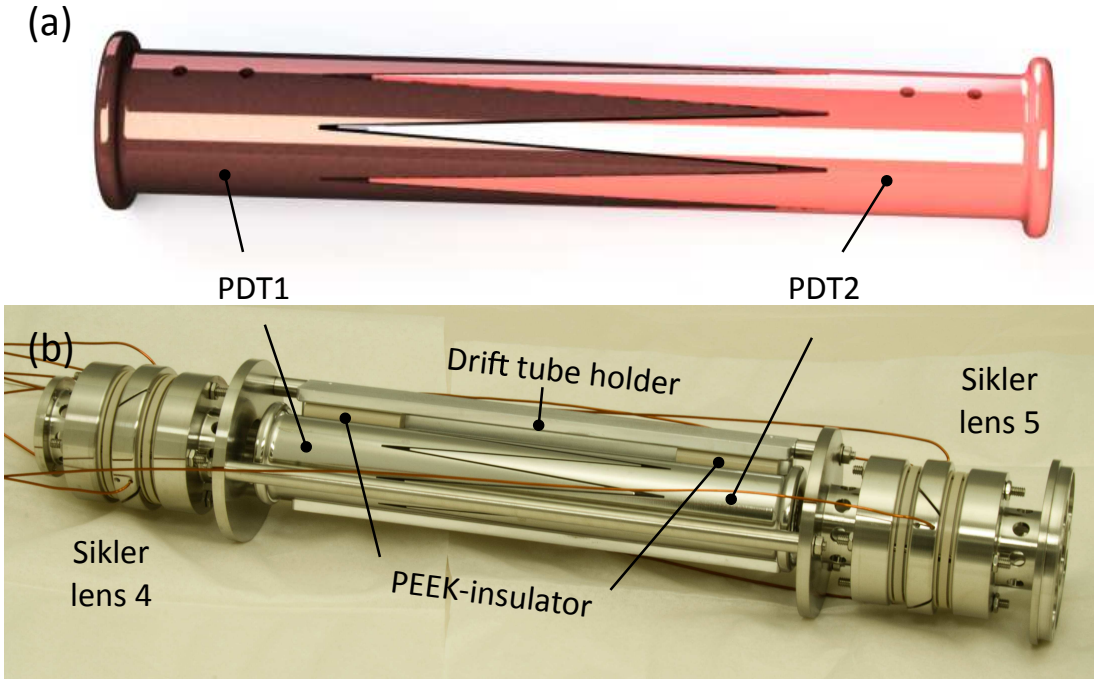

Figure 3.10: Cross section of the CAD model (a) and photograph (b) of the serrated PDTs that form the in-trap lift. In (b) two SLs, one on either side of the drift tube, SL 4&5, are additionally pictured, as well as the Kapton insulated copper electric wiring and the mechanical mount, made of aluminum and PEEK. Applying different voltages to PDT 1 and PDT 2, the serration of the two electrodes leads to a linear change in potential along the ion beam axis.

3.2.3 Pulsed drift tube

The pre-cooling unit, named pulsed drift tube (PDT), is essentially an in-trap lift cut in half to form a nearly linearly increasing potential along the beam axis. This is achieved by forming a serration between the two parts of the cylindrical electrodes and applying different voltages on them, as pictured in Figure 3.10. As their share in circumference changes linearly from one electrode to the other, the potential on the beam axis increases, as confirmed by simulations shown in Figure 3.11. The tube parts are clamped onto an aluminum u-profile with two alumina washer insulated screws each, two PEEK-cylinders providing insulation and cushioning between the profile and tube on each side. The screws provide the electrical connection leading to Kapton insulated wires. They are offset in the

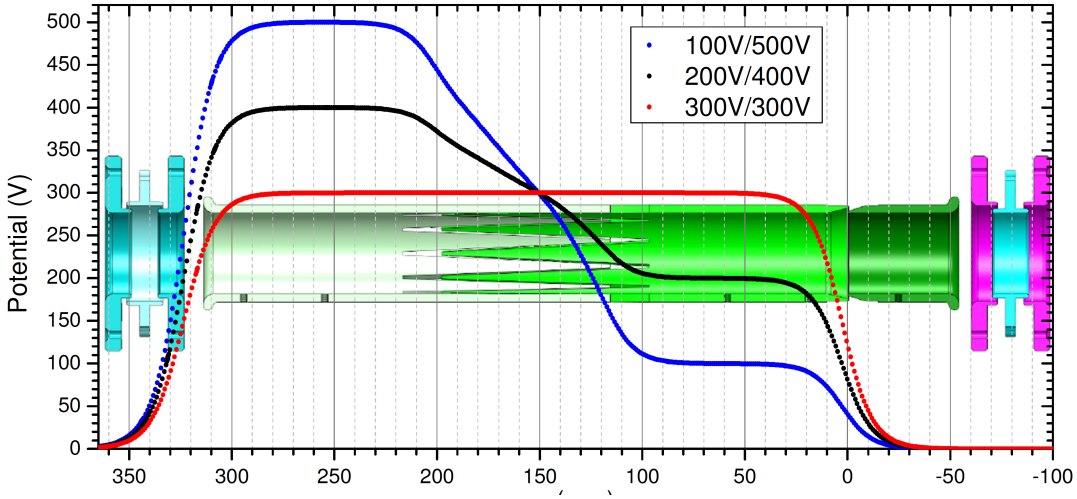

Figure 3.11: Simulation of the electrostatic potential of the PDTs on the ion beam axis. In its central region, the potential increases roughly linearly from the lower to the higher potential applied on the respective electrode. Taken from [30].

axial direction from one another, allowing for angular corrections of the tubes by adjusting their tightening torque. The other mounting angle is self-aligned by the symmetry of the u-profile and the tubes. Elongated holes in the u-profile allow for adjustment of the distance between both electrodes. The u-profile is fixed to the grounded parts of the surrounding SLs that are mounted into the vacuum chamber using centering apertures.

3.3 Diagnostics

In addition to the ion source and transport system, the experiment is equipped with diagnostic elements to characterize and optimize the beam of extracted ions. Since electrostatic elements do not allow spatial separation of different ions, as discussed in Section 2.2.1, position-sensitive diagnostics are only of limited interest. More interesting is the time resolution of incoming ions, so microchannel plate (MCP) detectors with a resolution up to ns were chosen. MCPs are thin, perforated plates ($\sim$ mm) made from a high resistance ($\sim 100\,\mathrm{M\Omega}$) material. The holes have a diameter of $\sim 50\,\mu\mathrm{m}$ and are inclined by $\sim 8°$. They act as miniature electron multipliers, amplifying the incoming ion signal by a cascade of secondary electron emission. Each of the detectors used here is composed of two such plates, stacked in the so-called Chevron configuration, with the inclination angle of their holes mirrored to each other, producing a chevron(Λ)-like shape. This allows an amplification factor of up to 1×10^7. [37]
The readout is realized by connecting the anode via a fast pre-amplifier to an oscilloscope. MCP 2 is additionally equipped with a retarding field analyzer in the form of two meshes in front of the MCP, as seen in Figure 3.12. The first mesh the ions reach is grounded, the second is set to a positive potential Φ_{Grid}, which is followed by the MCP as described above. Ions with an energy $E_{\mathrm{ion}} > qe\Phi_{\mathrm{Grid}}$ pass through both grids and reach the MCP, while the ions with less energy do not. This enables a direct measurement of the ion energy and energy spread.

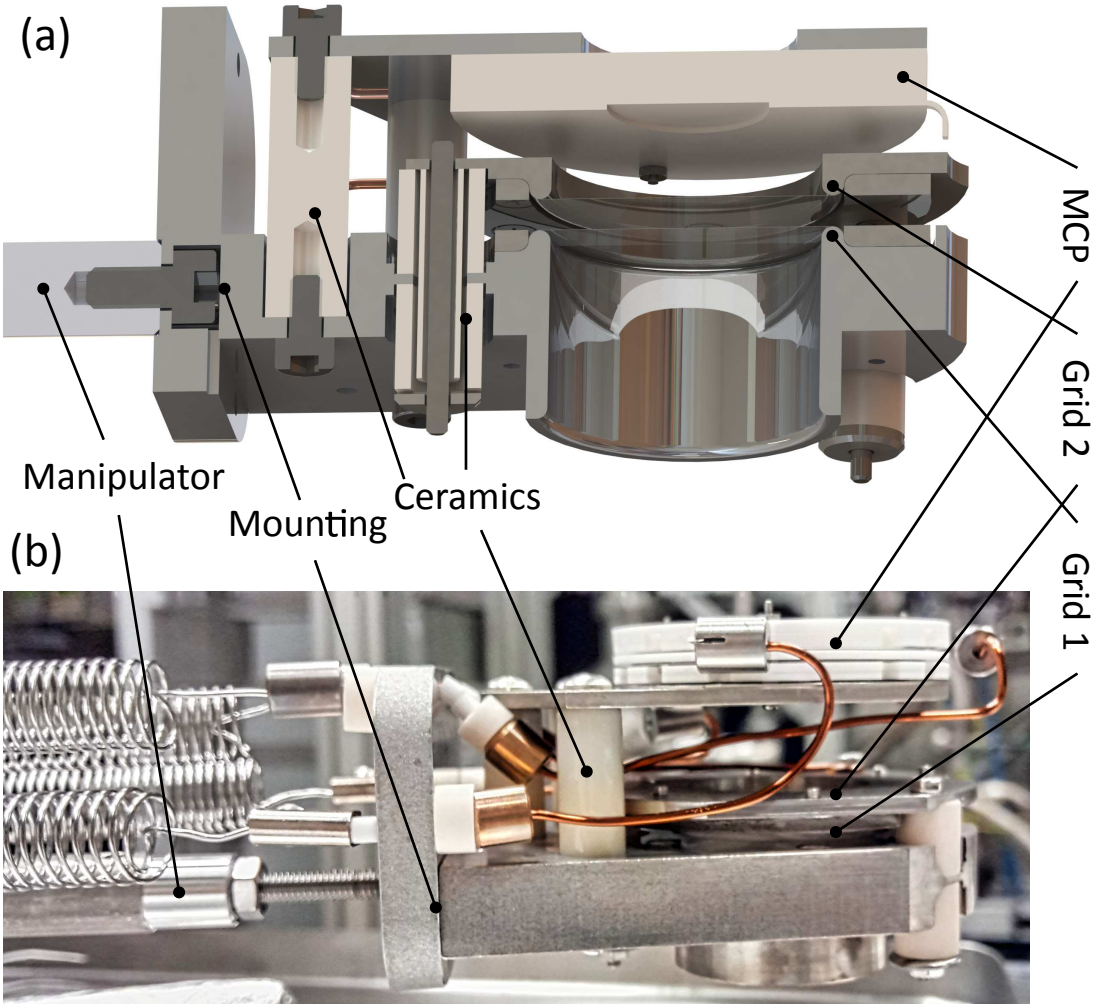

Figure 3.12: CAD model (a) and Photograph (b) of the mounted MCP detector with the retarding field analyzer. In (b) the electrical connection, in the form of springs, seen at the left, allows them to vary the length according to the position of the manipulator. There are four connections: MCP front, MCP back, MCP anode and Grid 2; Grid 1 is connected with the mounting and thus grounded.

3.4 Vacuum system

Ultra-high vacuum needs to be provided for the operation of the EBIT and beamline to decrease contamination, allow a high electron current and prevent recombination with background gas, especially after extraction. For this purpose, the experiment features a three-stage pumping system. The first stage is a scroll type roughing pump to reach a pressure below 1 mbar, allowing small turbo-molecular pumps to start to work. At the end of this stage sits an electromagnetic valve that closes in case of a power outage preventing the experiment to vent involuntarily. The second stage is an 80 L turbo-molecular pump, which reduces the pressure to below 1×10^{-3} mbar, allowing for the operation of 300 L turbo-molecular pumps. From here the vacuum system branches in two parts, one for EBIT and one for the beamline, both separable from the pump by a hand valve. They then connect to several 300 L turbo-molecular pumps that represent the third stage and are mounted on the main vacuum chambers. The exhaust of the pump of the gun chamber is equipped with a hand valve as well to shield off the gun separately. Here, pressures lower than 1×10^{-8} mbar in the beamline and 1×10^{-9} mbar in the EBIT are achieved, which are sufficient for operation. The higher pressure in the beamline is mostly due to out-gassing of different materials used, notably PEEK and Kapton, and the limitation to indirect pumping of the PDT chamber caused by architectural constraints, and is assumed to reduce further over time. Within the main chambers three gate valves are installed: One after the beamline, to attach it to the receiving trap, one between EBIT and beamline to allow for independent venting in case of repairs or extensions and one inside the EBIT - between main and gun chamber - to enable retracting the gun for protection of the cathode, allowing it to stay under vacuum while the remaining EBIT is vented.

3.4.1 Bellows

The beamline overview in Figure 3.1 forgoes the depiction of vacuum chambers, as they are not essential for the operating principles of the experiment. An exception has been made for the two bellows, one between SL 1 and SL 2 and one between SL 3 and SL 4. They are shown because they help to provide another important feature of the beamline: vibration decoupling. The decoupling takes place in two stages, whereas the chamber of the bender - enclosing SL 2 and SL 3 as well - forms the first stage and the PDT chamber,

additionally containing SL 4 and SL 5, the second. To minimize the coupling across the bellows, they are mounted in their equilibrium length. Besides segregating the chambers among themselves using bellows, dampening vibrations is realized by not mounting these chambers on the experiment frame and therefore to the floor directly. For the first stage, the bender, rubber buffers are sufficient, while the second stage is mounted on the rack of the receiving trap which is cushioned pneumatically. This reduces the disturbance of the trap mounted after the beamline, which will not be elaborated in more detail as it is not part of this experiment.

Chapter 4

Measurements

The following measurements taken for this work outline the generic proceedings for highly charged ion (HCI) production, extraction, transportation, selection, deceleration and bunching with the objective of preparation for re-trapping. Boron-like argon, $q = 13$, was chosen for this purpose as it is straightforward to produce and has proven to work for the predecessor beamlines [21, 22, 31, 30, 35]. After the optimization of the first extraction signal on the first microchannel plate (MCP 1), the charge states of the extracted ions will be determined by a differential time of flight (ToF) analysis for multiple extraction rate. An additional result of this measurement is the extraction rate with a sufficient ion yield of a given charge state. The resulting identification allows further selection of a single charge state - in this case, Ar^{13+} - by switching fast ion-optical elements in coincidence with the ion ToF. This is done by employing the bender, optimizing the remaining Sikler lenses (SLs 3-5) and additionally utilizing SL 3 as selection electrodes. The time delay between extraction and selection time is assessed. The isolated bunch is subsequently decelerated and bunched using the pulsed drift tubes (PDTs), evaluating the ToF and energy distribution of the decelerated bunch to examine a suitable switching time and voltage difference.

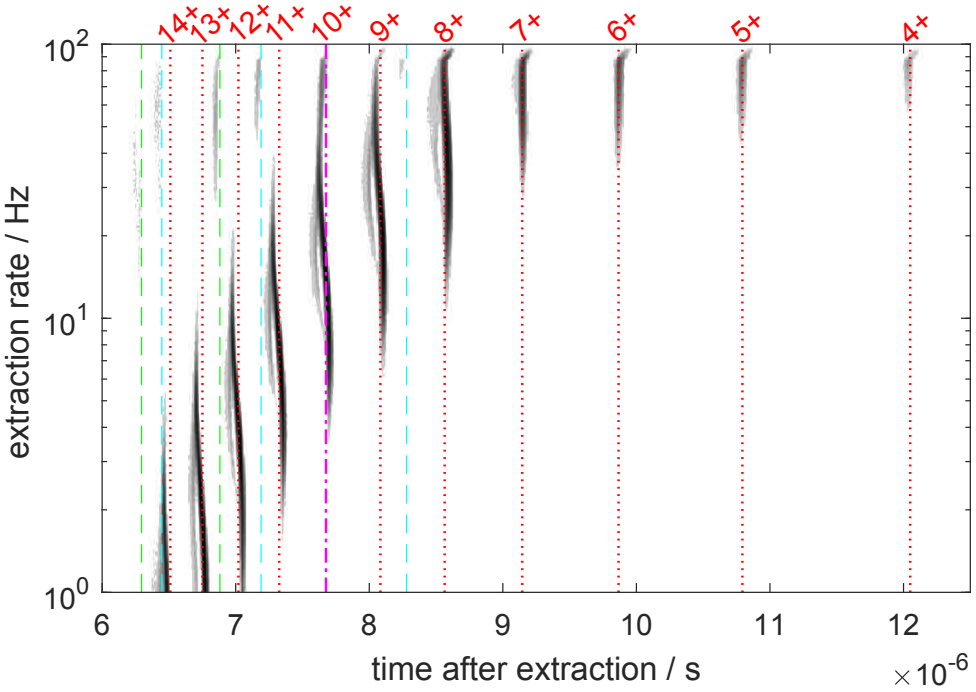

Figure 4.1: Time of flight signal for 250 different extraction rates between 1 Hz and 100 Hz as seen on MCP 1. The Argon injection pressure was $\sim 1.65 \times 10^{-7}$ mbar. Data above 50 Hz is unreliable, as the trap did not have enough time to completely reset. The slight change in time of flight for different extraction rates is presumably due to space charge effects. The bifurcation is supposedly caused by different ion paths through the SLs. The q/m analysis reveals Ar^{14+} to Ar^{4+} (red, dotted), as well as O^{4+} to O^{6+} (green, dashed) and N^{3+} to N^{5+} (turquoise, dashed). Argon charge states are given above. Note the overlay of O^{4+} with Ar^{10+} due to the same charge-to-mass ratio $q/m = 1/4\,e\,\mathrm{u}^{-1}$ (purple, dot-dashed). As expected, the lighter elements only occur at high extraction rates.

4.1 Charge state identification

To calibrate the ToF spectra argon is injected with $\sim 1.65 \times 10^{-7}$ mbar pressure in the injection system and extracted with the same electron beam ion trap (EBIT) settings at different extraction rates, equivalent to different breeding times. It is operated at ~ 100 V trap depth, ~ 850 V electron beam energy and ~ 6.5 mA electron beam current. For extraction, the potential of the central drift tube (DT) was raised to 650 V. This results in a series of ToF spectra including different charge states, e.g. the ten different states depicted in Figure 4.1. Turning the injection on and off during test measurements further confirms that the ion impinging on the MCP belong to different charge states of highly charged argon. One can see some shift towards longer ToF within a given charge state for lower extraction rates, probably due to space charge effects. Additionally, bifurcations, seemingly due to different flight paths through the ion optics occur. Nevertheless, these effects are small compared to the change in ToF due to different charge-to-mass ratio q/m. It is therefore sufficient to determine the mean ToF of each charge state of the spectra in Figure 4.1 by summing up all spectra to a single ToF spectrum. Subsequently, multiple Gaussians were fitted to get the average ToF of each peak as seen in Figure 4.2. The thus determined MCP 1 arrival times t follow equation 2.32, with an additional offset t_0 to account for different possible time delays, like differing signal line lengths:

$$t = t_0 + \frac{t_{\mathrm{Ar}^{1+}}}{\sqrt{q}} \tag{4.1}$$

Since the charge state q of an ion can only be a discrete value and increases uninterrupted from the slowest to the fastest ion, we know the difference between the charge states $q_{\mathrm{diff}} \in \{0, 1, 2, 3, 4, 5, 6, 7, 8, 9, 10\}$, relative to the slowest measured charge state q_{min}, q can be expressed as

$$q = q_{\mathrm{diff}} + q_{\mathrm{min}}. \tag{4.2}$$

This leads to ten known combinations of q_{diff} and t, which are plotted in Figure 4.3 and fitted by

$$t(q_{\mathrm{diff}}) = t_0 + \frac{t_{\mathrm{Ar}^{1+}}}{\sqrt{q_{\mathrm{diff}} + q_{\mathrm{min}}}} \tag{4.3}$$

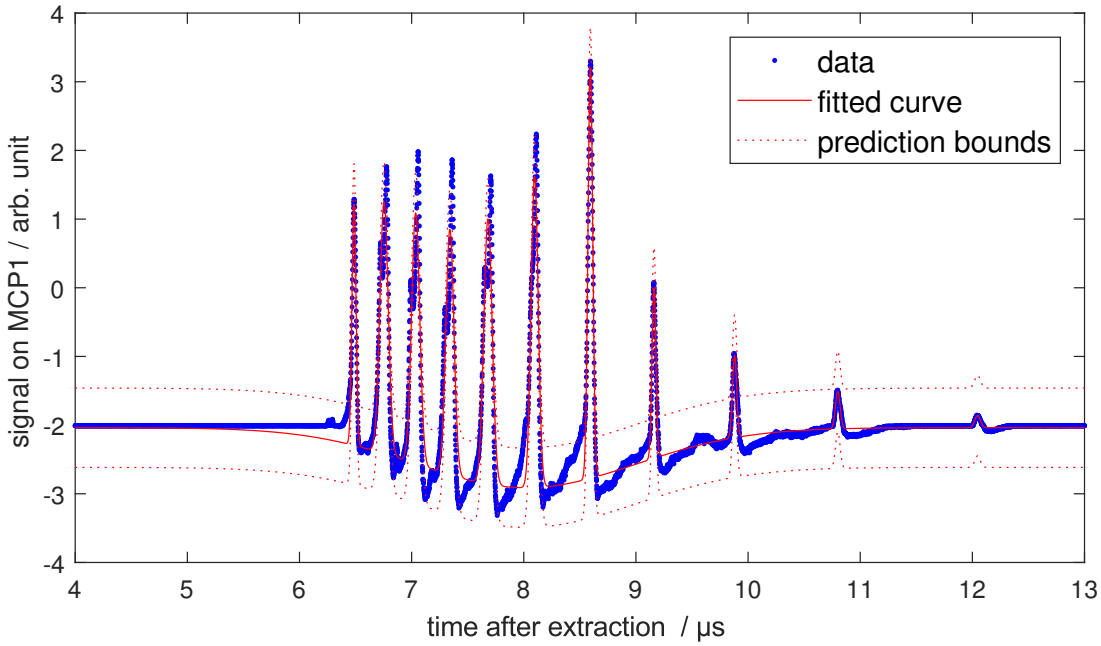

Figure 4.2: Projection of Figure 4.1 onto the "time after extraction"-axis by summing up each time bin. A background compensation function and multiple Gaussians were fitted to determine the mean ToF for each charge state.

to evaluate the depended parameters

$$q_{\min} = 4.15(6), \tag{4.4}$$
$$t_0 = -0.033(74)\,\mu\text{s}, \tag{4.5}$$
$$t_{\text{Ar}^{1+}} = 24.59(32)\,\mu\text{s}. \tag{4.6}$$

Since charge states can only take integer multiples of e the lowest charge states can be set to exactly $q_{\min} = 4$, as $q_{\min} = 5$ is more than $14\,\sigma$ away. Repeating the fit with the known charge states leads to:

$$q_{\min} = 4, \tag{4.7}$$
$$t_0 = 0.152(25)\,\mu\text{s}, \tag{4.8}$$
$$t_{\text{Ar}^{1+}} = 23.82(7)\,\mu\text{s}. \tag{4.9}$$

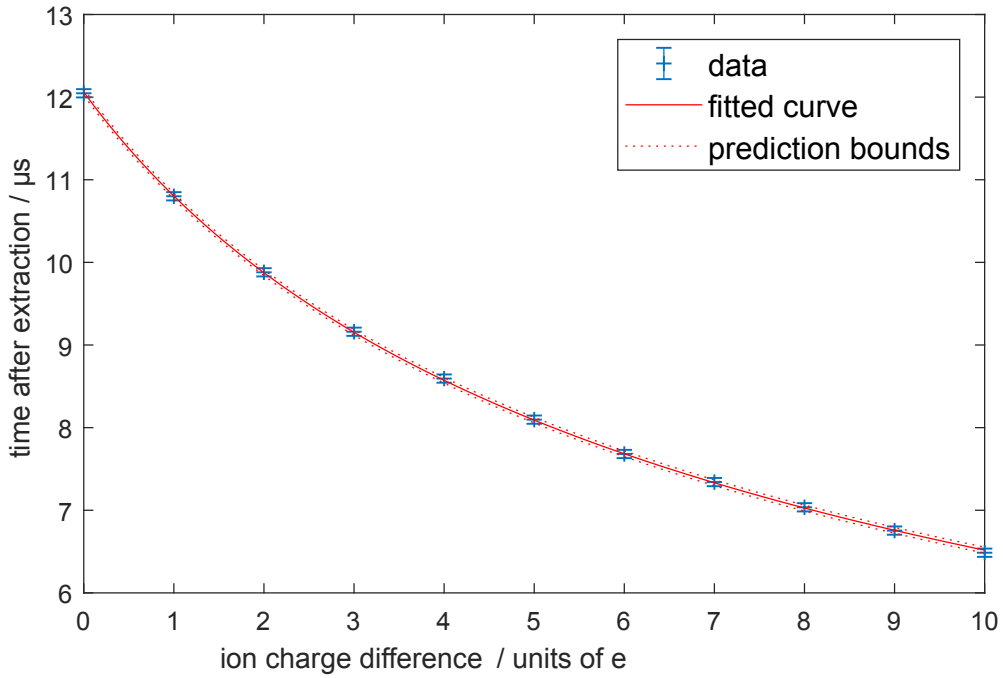

Figure 4.3: Ion arrival time on MCP 1 after extraction as determined in Figure 4.2 for different argon charge states. Only the charge state difference q_{diff} - exactly 1 between adjacent peaks - is known and used as abscissa. Equation 4.3 was fitted to evaluate the absolute charge states as well as the time offset t_0 and $t_{\text{Ar}^{1+}}$, the ToF of singly charged argon.

These values, as well as atomic mass data, were used to calculate various ToFs for different ions using equation 2.31, leading to the identification of various other ion signals visible in Figure 4.1, that were added as colored vertical lines. A complete overview of identified ion signals is given in table 4.1, including the ionization thresholds governing their production. These lie well within the reach of an electron beam energy of $\sim 850\,\text{eV}$, while the next charge state of Argon is out of reach - demanding $855.5(3)\,\text{eV}$ [38]. This further affirms the charge state identification.

Table 4.1: Detected ions in Figure 4.1. The times of arrival are calculated from fitting the argon ToFs, combining Equation 2.31 with the fit results in Equation 4.8 and 4.9, as well as atomic mass data. The ionization thresholds are taken from [38].

Ion	average time-of-arrival / µs	Ionization threshold of parent ion / eV
O^{4+}	7.676(33)	77.413 50(25)
O^{5+}	6.882(32)	113.8990(5)
O^{6+}	6.295(31)	138.1189(21)
N^{3+}	8.280(35)	47.4453(25)
N^{4+}	7.190(33)	77.4735(4)
N^{5+}	6.447(31)	97.8901(4)
Ar^{4+}	12.050(53)	59.58(18)
Ar^{5+}	10.794(40)	74.84(17)
Ar^{6+}	9.866(38)	91.290(10)
Ar^{7+}	9.146(37)	124.41(6)
Ar^{8+}	8.565(35)	143.4567(12)
Ar^{9+}	8.083(34)	422.60(6)
Ar^{10+}	7.676(33)	479.76(12)
Ar^{11+}	7.326(33)	540.4(6)
Ar^{12+}	7.021(32)	619.0(4)
Ar^{13+}	6.751(32)	685.5(3)
Ar^{14+}	6.511(31)	755.13(22)

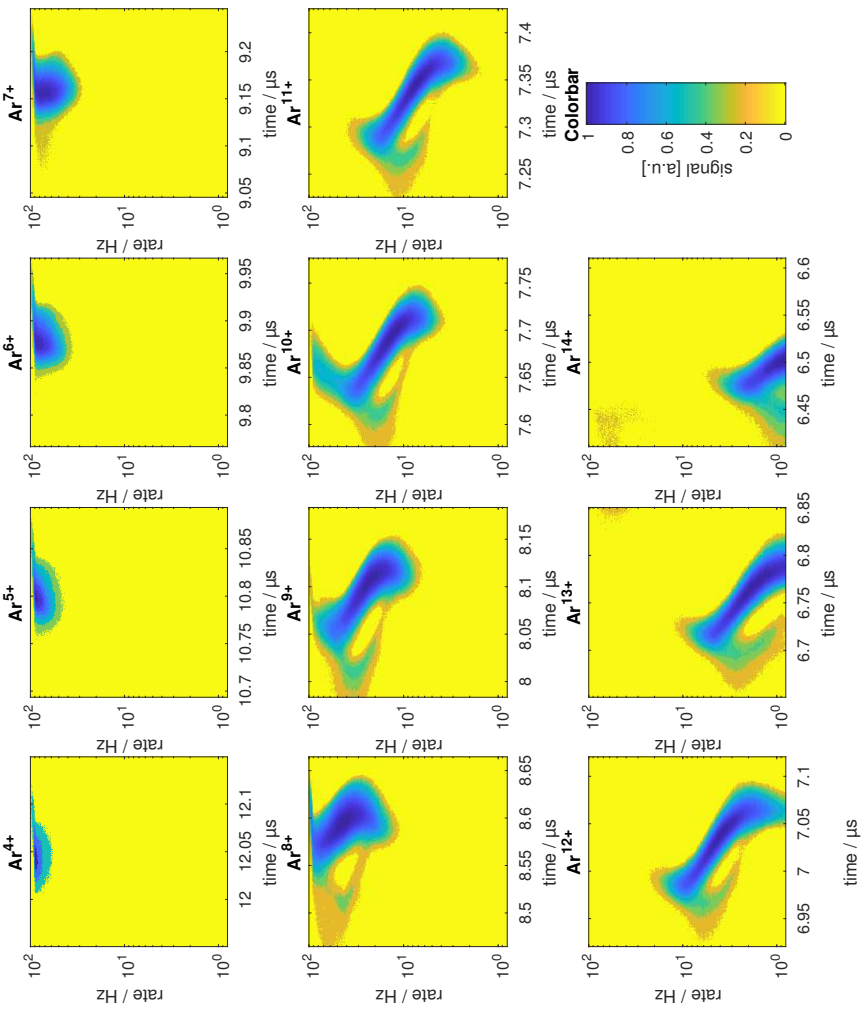

Figure 4.4: Slices of 0.2 µs taken from Figure 4.1 to define integration areas for each argon charge state, as labeled above each plot. One can clearly see the bifurcations and the overlay of Ar^{10+} with O^{4+} as mentioned above. Apart from that, no significant additional signal is present in any of the slices.

4.1.1 Breeding time influence

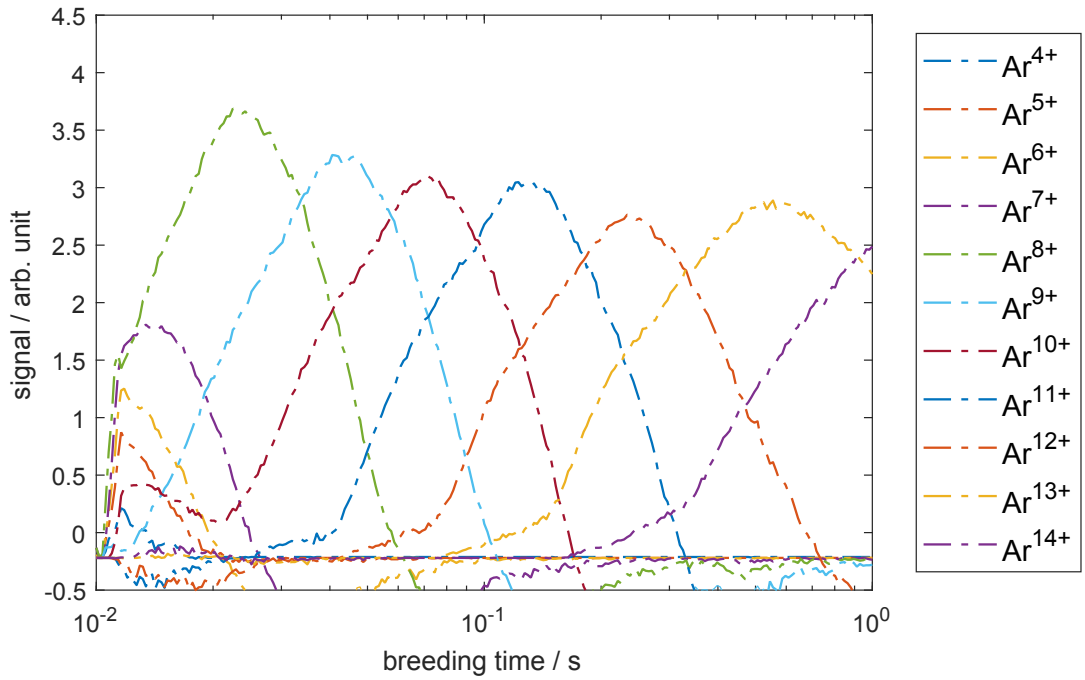

Figure 4.5: Charge state distribution of extracted argon ions for different extraction rates, based on the integration areas in Figure 4.4. The sequential nature of the ionization process is clearly visible, as charge stats steadily increase with the breeding time. Note that the additional increase for low breeding times in the Ar^{10+} line arises from O^{4+}. The results are in agreement with the theoretical distribution in Figure 2.2.

The data analyzed in Section 4.1 can be further used to find a suitable extraction rate for specific charge states of argon. In order to do so, the spectra were divided into 0.2 µs long slices around the different argon charge state arrival times stated in table 4.1, as they include most of the signal of a given charge state and near to no other signal, except for the Ar^{10+} / O^{4+} overlay. This is displayed in Figure 4.4. Thereafter, individual slices are projected onto the extraction rate axis, summing up the signal of the given charge state equivalently to integrating the signal. The resulting charge state distribution is portrayed in Figure 4.5, where the reciprocal of the extraction rate, the breeding time, was chosen as the x-axis. The breeding time needed for a certain charge state increases exponentially

for a given charge state, within the boundaries of the experimental setup and the electron beam energy. This agrees well with theoretical predictions shown in Figure 2.2 and will be kept in mind as the operational parameters are optimized for the production and extraction of Ar^{13+}, which has an optimal extraction rate around $\sim 5\,\mathrm{Hz}$ for the EBIT settings used here.

4.2 Charge state selection

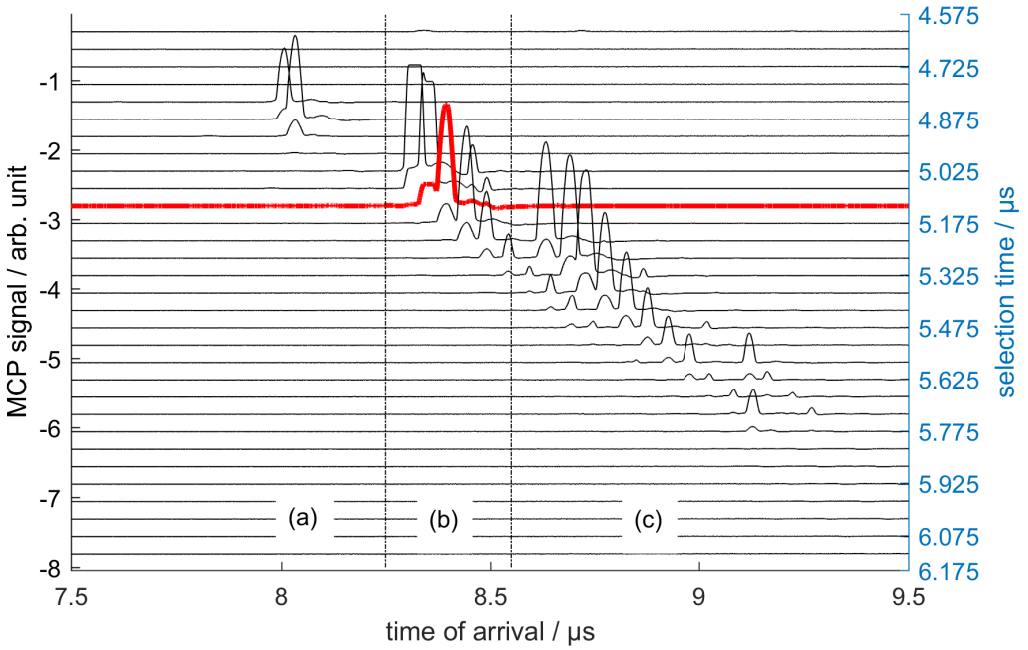

Figure 4.6: Visualization of the charge state selection process. Each line represents the MCP 2 signal (black axis, left) taken for a different position of the 0.400 µs long selection window (blue axis to the right). Depicted is the change between the charge states (a) $q = 14$ (b) $q = 13$ and (c) $q = 12$ The signal of the subsequent applied selection time of 5.125 µs is drawn in red. The small hump in the front only corresponds to the same ions taking a different path to the ion optics as mentioned above.

Keeping the settings from before, it was decided to use electrodes from SL 3 to select the desired charge state. The main reasons are that at that distance the charge state separation is already adequate for selection and no other ion optical element follows directly behind it, reducing the necessary deviation from the ideal path to assure ions hit the wall. The second part of the beamline, composed of the bender, SL 3-4 and the PDTs, was turned on and used to optimize the signal on MCP 2. The extraction voltage was increased to 1000 V, followed by a re-optimization of the whole beamline, to further increase the ion yield. Both PDTs were set to $U_{\mathrm{PDT1}} = U_{\mathrm{PDT2}} = 700\,\mathrm{V}$ to minimize the changes needed to implement the energy reduction later on as the ions are already focused through the PDTs.

Omitting SL 5 is based on its low influence on the signal, caused by its short distance to MCP 2, which also later permits a degree of freedom in focusing the decelerated ions into the next element after the beamline. The EBIT was operated with the same settings as above with an extraction rate of 5 Hz, delivering a high amount of Ar^{13+} and medium amounts of Ar^{12+} and Ar^{14+}, demanding a selection of the middle bunch. The distance to MCP 1 and SL 3 from the EBIT is just about the same and the bunch separation as seen above is roughly $\sim 0.250\,\mu s$, with bunch lengths of about $\sim 0.130\,\mu s$, for charge states of $\sim 13\,e$. It was therefore decided to use a transmitting voltage setting with a window of $0.400\,\mu s$ leading to the ideal ion path, and non-transmitting voltage setting which causes the ion path to hit the vacuum chamber were used otherwise. The selection time was scanned to identify the ideal one, as can be seen in Figure 4.6. Since the middle bunch with the least possible contamination is desired, a switching time of $5.125\,\mu s$ was used for the following experiments. The corresponding ToF spectrum is marked in red. It features a clear, strong signal from $q = 13$ without any occurrence of a signal from different charge states.

4.3 Energy reduction

4.3.1 Switching time

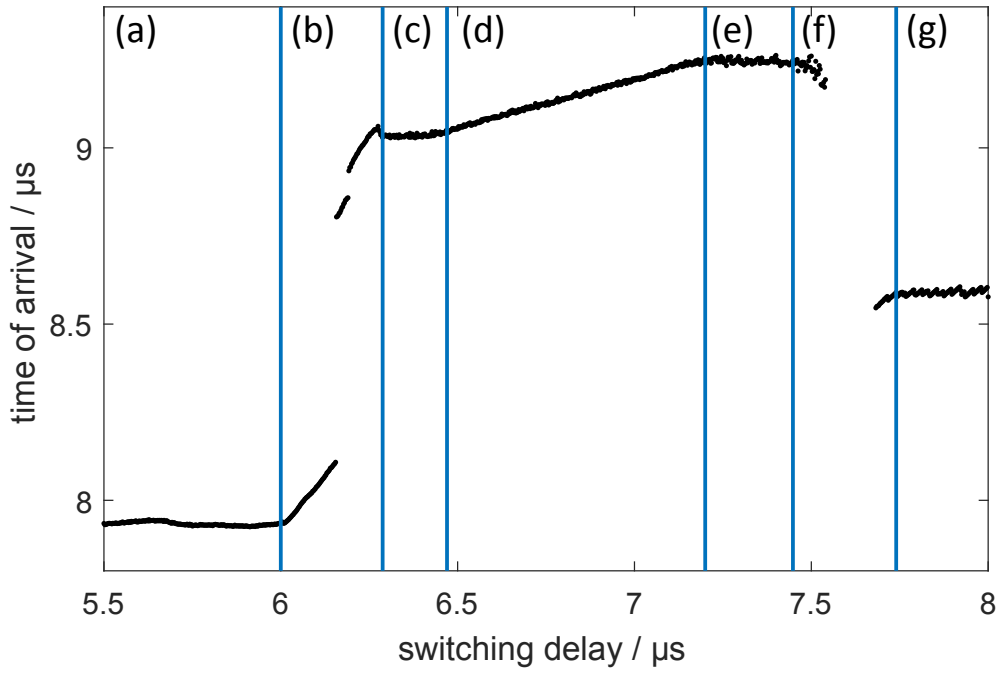

Figure 4.7: Mean time-of-arrival of Ar^{13+} ions on MCP 2 for different PDT switching times. The designated areas correspond to different positions of the ions at that point in time: (a) before the PDTs, (b) entrance of PDTs, (c) undivided part of PDT 1, (d) serrated part of the PDTs, (e) undivided part of PDT 2, (f) exit from PDTs, (g) after the PDTs.

With the correct charge state selected, the next step is to implement the deceleration with the PDTs. The focusing into its electrodes was already guaranteed above. They are now switched from $U_{\mathrm{PDT1}} = U_{\mathrm{PDT2}} = 700\,\mathrm{V}$ to ground potential. This slows down the ions and allows the optimization of SL 5 to get a stronger signal from the decelerated ions. The time for switching is set roughly between the selection time and the arrival time from Figure 4.6, i. e. $\sim 5.1\,\mu\mathrm{s}$ and $\sim 8.4\,\mu\mathrm{s}$, to $6.75\,\mu\mathrm{s}$. Evidence that this very rough estimation is justified is provided by the fact that the ToF gets, as anticipated, larger. This might also be the case for switching the PDTs while the ions are at their entrance or exit - an

assumption that is disproven by the possibility of changing the deceleration time slightly, e. g. to 6.7 µs or 6.8 µs, without influencing the ToF.
Lowering U_{PDT1} to ~600 V to produce a linear potential inside the PDTs, the switching time is improved further by increasing it by steps of 2.5 ns, each step taking a ToF spectrum and determining the time for the maximal signal on MCP 2, resulting in Figure 4.7. It is divided into seven different parts, corresponding to different spatial ion positions at the time of the switching, as the different position also means a different potential that is lost, compare Figure 3.11:

(a) The ions have not reached the PDT electrodes yet. They are therefore not decelerated and arrive fastest at the MCP and are independent from small perturbations.

(b) They are near the entrance of the PDT electrodes. The potential changes rapidly from ground potential to the potential of PDT 1 - and so does the time-of-arrival.

(c) The flat potential of the beginning of PDT 1 is experienced since the serrated part has not begun yet.

(d) The serrated part is reached where the geometrical proportion of circumference changes linearly from PDT 1 to PDT 2. Subsequently, the potential follows roughly linearly, resulting in a somewhat linear increase in the time-of-arrival.

(e) After the serrated part, the flat potential of PDT 2 predominates. Note that this region is longer in units of time than (iii), although the PDTs are structurally symmetrical since there is a higher potential and the ions are therefore slower.

(f) The ions reach the exit of the PDTs and the potential changes rapidly. Note some missing data points where the signal was so weak that no maximum could justifiably be determined.

(g) Having left the influence of the PDTs completely, the ions are on ground potential. Although they undergo no net deceleration, i. e. do not lose energy, they arrive later than in (i) since they now have to traverse the PDTs while they are on potential, suffering deceleration and acceleration along the way, lengthening their effective path-length.

The ideal switching time is now determined by taking the average time-of-arrival in region (iii) 9.0338(32) µs and (v) 9.2460(65) µs, taking the average from both values - 9.1399(72) µs - and determining the switching delay corresponding to this time-of-arrival in region (vi), 6.801(48) µs, by fitting and evaluating a linear function.

4.3.2 First energy analysis

Applying a switching delay of 6.8 µs, the retarding field analyzer, Section 3.3, was employed to measure the energy distribution of the ion bunch. This is done by increasing the voltage on grid 2 (U_{Grid}), in steps of 4 V and integrating the MCP signal for each step. This measurement was done with grounded PDTs as well as with $U_{\mathrm{PDT1}} \approx 600\,\mathrm{V}$ and $U_{\mathrm{PDT2}} \approx 800\,\mathrm{V}$, the result is shown in Figure 4.8. This type of measurement results in a cumulative energy distribution function. Assuming a Gaussian energy distribution for the ion bunches, this corresponds to the error function. As a consequence,

$$\mathrm{signal}(U_{\mathrm{Grid}}) = A\left(1 - \mathrm{erf}\left[\frac{U_{\mathrm{Grid}} - \bar{U}}{\sqrt{2}\,\sigma}\right]\right) \tag{4.10}$$

is fitted to the measurements, resulting in

$$A = 134.9(12)\,\mathrm{arb.\,unit}, \tag{4.11}$$
$$\bar{U} = 929.33(36)\,\mathrm{V}, \tag{4.12}$$
$$\sigma = 8.40(50)\,\mathrm{V}, \tag{4.13}$$

for the untreated bunch and

$$A = 75.56(37)\,\mathrm{arb.\,unit}, \tag{4.14}$$
$$\bar{U} = 225.14(21)\,\mathrm{V}, \tag{4.15}$$
$$\sigma = 2.80(32)\,\mathrm{V}, \tag{4.16}$$

for the decelerated bunch.
This shows a net reduction of energy spread from $\Delta E_{\mathrm{ion}}/q = 8.40(50)\,\mathrm{eV}$ to $\Delta E'_{\mathrm{ion}}/q = 2.80(32)\,\mathrm{eV}$. The MCP signal amplitude reduces from 134.9(12) arb. unit to 75.56(37) arb. unit, a ratio of 0.5601(57). This is well inside the range expected due to the velocity dependence

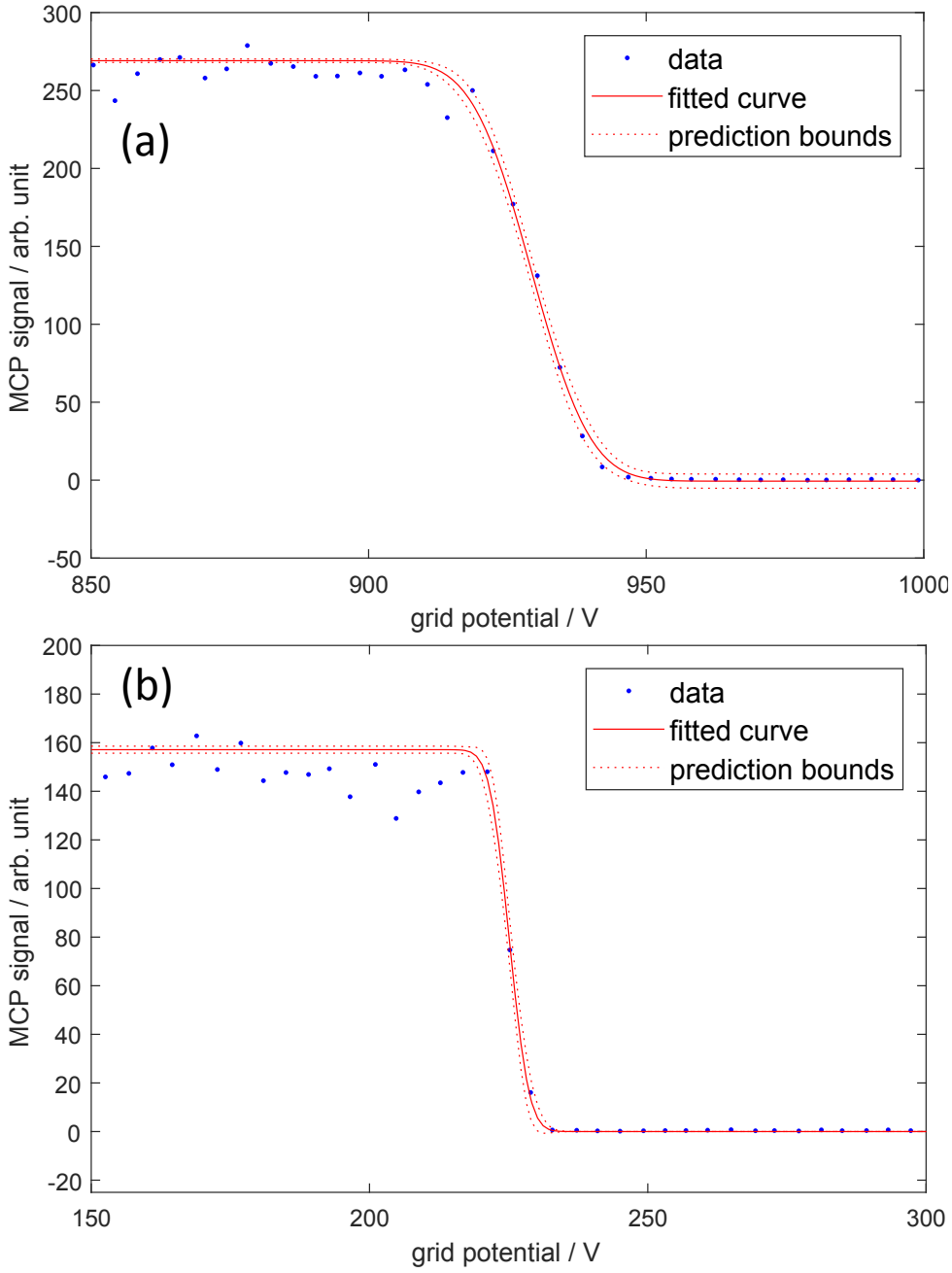

Figure 4.8: Cumulative energy distribution of Ar^{13+} ion bunches measured with the retarding field analyzer at MCP 2 before (a) and after deceleration (b). Both the mean energy and the energy spread are reduced. The lower amplitude for the decelerated ions does not necessarily indicate ion loss since the MCP gain increases with ion velocity. Data acquisition and fit encompass grid potentials in the range of 0 V to 1 kV for both, (a) and (b), but only the crucial sections of the abscissa are shown here for ease of comparison.

of the MCP gain [39]. For the same reason, the precise difference in ion number before and after deceleration can not be determined. The difference of mean ion energy per charge state is

$$E_{\text{ion}}/q = 929.33(36)\,\text{eV} - 225.14(21)\,\text{eV} = 704.19(41)\,\text{eV}, \tag{4.17}$$

in agreement with a mean PDT voltage of ∼700 V.

4.3.3 Optimization of voltage differences

The remaining ion energy is reduced by applying a DC voltage bias on the supplied trap. For technical reasons this voltage might be limited, e.g. to 200 V as for the Paul trap used in [31]. The mean ion energy is therefore reduced even further by applying a mean PDT voltage $\bar{U}_{\text{PDT}} = (U_{\text{PDT1}} + U_{\text{PDT2}})/2 = 800\,\text{V}$. Furthermore the voltage difference $\Delta U_{\text{PDT}} = \bar{U}_{\text{PDT}} - U_{\text{PDT1}} = U_{\text{PDT2}} - \bar{U}_{\text{PDT}}$ is scanned in steps of 2 V from 100 V to 200 V to minimize the energy spread. For each U_{PDT} combination, U_{Grid} is swept from 100 V to 200 V in 1 V steps, integrating the MCP signal in the appropriate time range for all U_{PDT}-U_{Grid} combinations. The resulting energy distributions are plotted in Figure 4.9, each was analyzed as outlined in Section 4.3.2. The fitting function has been slightly altered to regard the additional signal drop around ∼145 V, essentially to only treat the last edge of the U_{Grid}-scan. The drop is presumably caused by a moiré effect between the two grids of the retarding field analyzer and will be discussed later. It can not describe the actual energy distribution since the cumulative distribution is measured and therefore must be continuous. The results of these fits are displayed in Figure 4.10. The chosen lines in Figure 4.9 (b) mark the changing behavior of the deceleration process and are therefore indicated in Figure 4.9 (a) and 4.10 as well. The observed behaviors are:

$\Delta U_{\text{PDT}} \leq 126\,\text{V}$, up to cyan:

Increasing signal amplitudes, probably due to better acceptance of the PDTs for lower U_{PDT1}. While at first glance it looks like a vast reduction of the mean energy with constant energy spread, this is not the case. It is rather an artifact caused by the overlay of the actual energy spread and the signal drop around ∼150 V. The fitting algorithm can not distinguish both signal reductions and combines them. Therefore the resulting "energy spread" is more a measure of the combined declination width than the actual ΔE. The reduced ΔE causes the right edge in Figure 4.9 (a) to move to the left, leading to a decreased $\bar{U}$.

$126\,\mathrm{V} < \Delta U_{\mathrm{PDT}} \leq 138\,\mathrm{V}$, cyan to blue:

The energy spread of the ion bunch becomes distinguishable from the moiré effect. The mean energy goes to an approximately constant while the energy spread steadily drops. The slight decrease in signal amplitude might be due to saturation effects, as the bunched ions arrive in a smaller and smaller time window, leading to increasing electron depletion in the MCP.

$138\,\mathrm{V} < \Delta U_{\mathrm{PDT}} \leq 150\,\mathrm{V}$, blue to red:

The smallest energy spreads achievable with this setup are reached here, with the minimum at

$$\Delta U_{\mathrm{PDT}} = 140\,\mathrm{V}, \tag{4.18}$$

$$A = 87.26(23)\,\text{arb. unit}, \tag{4.19}$$

$$\bar{U} = 163.27(12)\,\mathrm{V}, \tag{4.20}$$

$$\sigma = 3.22(13)\,\mathrm{V}. \tag{4.21}$$

$150\,\mathrm{V} < \Delta U_{\mathrm{PDT}} \leq 182\,\mathrm{V}$, red to magenta:

Here, the energy spread stays relatively low, but its uncertainty increases. This is the region where the initially slowest ions start to end up as the fastest, overtaking the others, resulting in unstable ion bunches. Energy spread increases slightly towards the end.

$182\,\mathrm{V} < \Delta U_{\mathrm{PDT}}$ magenta and above:

The initially slowest ions now end up with more and more energy, resulting in a higher energy spread than before deceleration. The signal arising at $\sim 180\,\mathrm{V}$ in Figure 4.9 is caused by this.

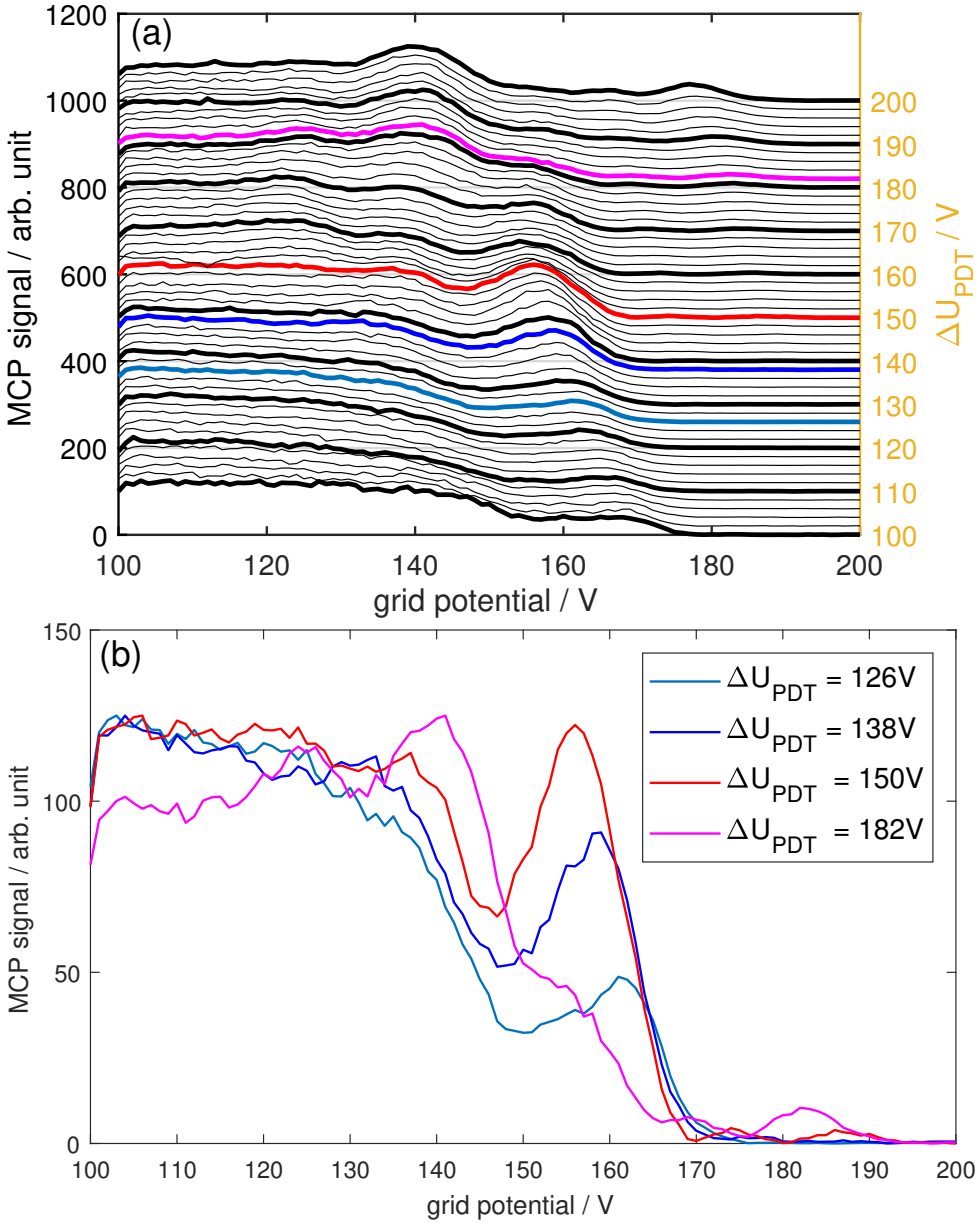

Figure 4.9: Visualization of the pre-cooling process. Each line in (a) represents the MCP signal (black axis, left) for different retarding grid potential, offset corresponding to ΔU_{PDT} (yellow axis, right). The color-marked lines, plotted again in (b) without offset, represent the transitions of different behaviors: For ΔU_{PDT} below 138 V, e.g. the cyan line, the potential slope is too small for ideal cooling. For ΔU_{PDT} between 138 V and 150 V the best cooling occurs, including red and blue. Above $\Delta U_{\mathrm{PDT}} = 150$ V ions overtake each other, as can be seen with the signal emerging at 180 V grid potential for the magenta line.

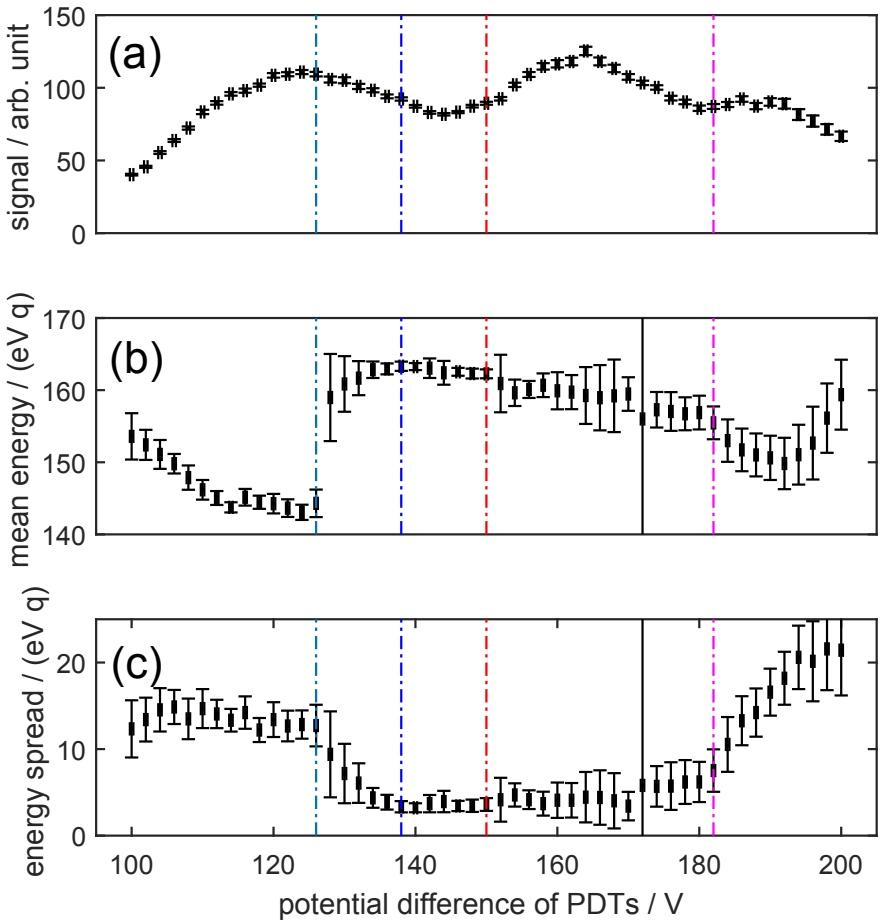

Figure 4.10: Evaluation of the pre-cooling process. (a) Signal amplitude, (b) mean energy and (c) energy spread determined for different ΔU_{PDT}. The colored lines mark the same representations as in Figure 4.9, while here the different cooling effect can explicitly be seen in (c). F.l.t.r: ΔE_{ion} constant high, decreasing, constant low, slightly increasing, steep increasing above initial spread.

Shape of the retarding field analyzer measurements

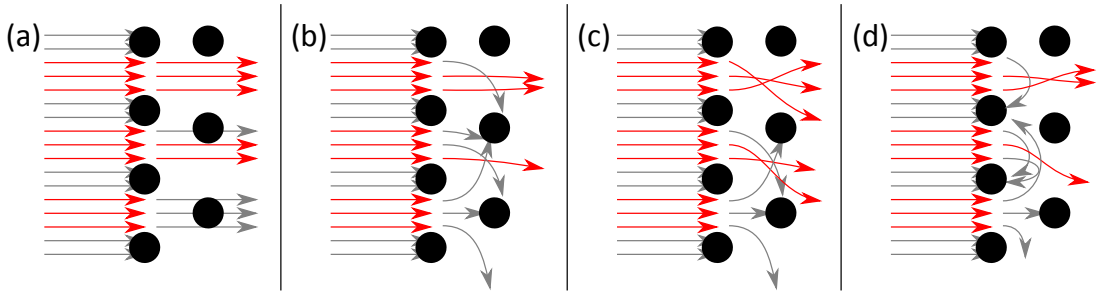

Figure 4.11: Possible explanation of the signal drop seen in Figure 4.9. Schematically imaged are the two grids of the retarding field analyzer (black circles) and representations of ion paths (red/gray arrows). Red arrows pass their respective grid, while grey ones do not. From (a) to (d) the potential on the second grid U_{Grid} increases relative to the ion energy, further repelling the ions. (a) Near to no perturbation to the ions paths, resulting in geometrical transmission behavior. (b) The incipient field deflects ions, preventing them passing the second grid, causing the transmission to decline. (c) With an even stronger field, ions get refocused, obtaining or even exceeding the geometrical transmission (d) The potential exceeds the ions' energy. Increasing potential leads to decreased transmission.

The used wire meshes for the grids of the retarding field analyzer have a geometric transmission of about $\sim 50\,\%$ each. As it is a soft, textile-like component, the alignment of one grid relative to the other changes for different positions on the grid: At some point, a hole in grid 1 would be over a wire in grid 2 and vice versa, while at another point hole is aligned with hole and wire with wire. Applying different potentials on the second grid may subsequently lead to various deflection and refocusing effects as illustrated in Figure 4.11. This could explain the discontinuous behavior of the signal seen in Figure 4.9 that cannot reflect an actual cumulative energy distribution.

Chapter 5

Résumé

Summary and Conclusion

The objective of this thesis was to build and characterize a source for Highly charged ions (HCIs) with a corresponding beamline to prepare them for ultra-cold environments. It was demonstrated that neutral argon could be injected in the electron beam ion trap (EBIT), ionized to the desired charge state $q = 13$ and extracted onto a microchannel plate (MCP) detector. Successful charge state identification, yield maximization and selection have been implemented. Deceleration, bunching and pre-cooling have been carried out effectively, resulting in slow, low-energy ions suitable for injection and re-trapping in the Paul trap. The EBIT was capable of generating argon ions of charge states up to $q = 14$ at $\sim 100\,\mathrm{V}$ trap depth, $\sim 850\,\mathrm{V}$ electron beam energy, $\sim 6.5\,\mathrm{mA}$ electron beam current and $\sim 1.65 \times 10^{-7}\,\mathrm{mbar}$ injection pressure. Initially, ions have been extracted straight onto MCP 1. For extraction with 650 V, the time-resolution was high enough to conduct a conclusive charge state identification. This was based on the evaluation of the measured time of flight (ToF) spectra, where ion separation due to their charge-to-mass ratio q/m occurs. The known ToF ratios of $t_\mathrm{i}/t_\mathrm{j} = \sqrt{q_\mathrm{j}}/\sqrt{q_\mathrm{i}}$, for ions of the same mass, have been utilized to identify the absolute charge states. The identification agrees with the known ionization thresholds for highly charged argon. The optimal breeding time for respective charge states increases exponentially, confirming theory predictions qualitatively. Quantitative deviations from the predicted breeding times are mainly caused by the estimation of the overlap of the electron beam and the ion cloud needed for the simulation. The mea-

surement of the charge state time evolution showed an optimal extraction rate of ∼5 Hz for the above-mentioned settings to yield Ar^{13+} ions. The ToF separation of individual charge states at the third Sikler lens (SL), directly behind the bender, has proven wide enough for charge state selection, isolating a single q/m species, in this case, Ar^{13+}, even for an increased extraction voltage of ∼1 keV. The ideal switching time for the pulsed drift tubes (PDTs) has been determined as well, resulting in the ion cloud being centered at the time of switching. The additional evaluation of the optimal PDT voltages - 660 V at PDT 1 and 940 V at PDT 2 - allowed for the reduction of the ion energy per charge state from $E_{\mathrm{ion}}/q = 929.33(36)\,\mathrm{eV}$ to $E_{\mathrm{ion}}/q = 163.27(12)\,\mathrm{eV}$ and of the energy spread per charge state from $\Delta E_{\mathrm{ion}}/q = 8.40(50)\,\mathrm{eV}$ to $\Delta E_{\mathrm{ion}}/q = 3.22(13)\,\mathrm{eV}$. The energies have been measured with the retarding field analyzer in front of MCP 2. These results are deemed sufficient for achieving efficient re-trapping in the Paul trap, based on the requirements outlined in [31, 30] for a similar setup.

Outlook

The next step is to align the beamline with the new superconducting Paul trap, which is being commissioned, and guide accordingly prepared HCIs through it, using its radio-frequency quadrupole field to refocus. After this is successfully done, electric mirror electrodes on either side of the trap can be used for re-trapping the HCIs, causing them to repeatedly traverse the trap. The maximal trapping time will be measured, allowing to draw conclusions about the recombination rate, due to interaction with background gases. Subsequently, co-crystallization with Be^{+} will be possible, once a laser-cooled Coulomb crystal has been prepared in the trap center, leading to sympathetic cooling. With this EBIT, not only are different charge states accessible, but also a variety of elements are available for gas injection. This and the electrostatic nature of the beamline make the setup versatile with regard to different charge-to-mass ratios. As a consequence, the setup can be used to survey the trapping characteristics of the Paul trap. Once the Paul trap has been characterized and sympathetic cooling including co-crystallization has been successful, one can implement precision spectroscopy. Ar^{13+} appears to be the ideal candidate for proof of principle measurements since not only is the beamline currently optimized for this HCI, but a spectroscopy laser is already available and the transition energy is well-known

from other experiments [22, 40, 41]. Future steps include the combination of the Paul trap with the XUV frequency comb which is currently commissioned at the institute [42]. This opens up the possibility of operating an atomic clock in the XUV regime, increasing the transition frequency as compared to optical clocks, further reducing the stability limitation caused by quantum fluctuations [13]. The capability of EBIT and beamline to provide a variety of HCIs and the wide range of wavelengths covered by the frequency comb opens up great opportunities for precision spectroscopy.

Appendices

Bibliography

[1] T. W. Hänsch, "Nobel lecture: Passion for precision," *Rev. Mod. Phys.*, vol. 78, pp. 1297–1309, Nov 2006.

[2] P. Duhem, *Physical Theory and Experiment*, pp. 1–40. Dordrecht: Springer Netherlands, 1976.

[3] Measurement Science Conference, "History of metrology." Available: `http://msc-conf.com/history-of-metrology` [2019, Oct], 2019.

[4] J. Wilkins, *An essay towards a real character and a philosophical language /by John Wilkins D.D. Dean of Ripon, and fellow of the Royal Society.* London: Printed for Sa. Gellibrand, and for John Martin, 1668.

[5] Bureau International des Poids et Mesures, "Member states / 1875." Available: `https://www.bipm.org/en/about-us/member-states/original_seventeen.html` [2019, Oct] BIPM, Sèvres, France.

[6] Bureau International des Poids et Mesures, "History of the SI." Available: `https://www.bipm.org/en/measurement-units/history-si/` [2019, Oct] BIPM, Sèvres, France, 2019.

[7] W. A. Marrison, "The evolution of the quartz crystal clock," *Bell Labs Tech. J.*, vol. 27, pp. 510–588, July 1948.

[8] D. Sobel and W. Andrewes, *Längengrad - die illustrierte Ausgabe: die wahre Geschichte eines einsamen Genies, welches das größte wissenschaftliche Problem seiner Zeit löste.* Berlin-Verlag, 2010.

[9] M. Lombardi, T. P. Heavner, and S. Jefferts, "Nist primary frequency standards and the realization of the si second," *NCSLI Measure J. Meas. Sci.*, vol. 2, pp. 74–89, Dec 2007.

[10] G. Santarelli, P. Laurent, P. Lemonde, A. Clairon, A. G. Mann, S. Chang, A. N. Luiten, and C. Salomon, "Quantum projection noise in an atomic fountain: A high stability cesium frequency standard," *Phys. Rev. Lett.*, vol. 82, pp. 4619–4622, Jun 1999.

[11] T. P. Heavner, E. A. Donley, F. Levi, G. Costanzo, T. E. Parker, J. H. Shirley, N. Ashby, S. Barlow, and S. R. Jefferts, "First accuracy evaluation of NIST-F2," *Metrologia*, vol. 51, pp. 174–182, May 2014.

[12] W. M. Itano, J. C. Bergquist, J. J. Bollinger, J. M. Gilligan, D. J. Heinzen, F. L. Moore, M. G. Raizen, and D. J. Wineland, "Quantum projection noise: Population fluctuations in two-level systems," *Phys. Rev. A*, vol. 47, pp. 3554–3570, May 1993.

[13] R. J. Rafac, B. C. Young, J. A. Beall, W. M. Itano, D. J. Wineland, and J. C. Bergquist, "Sub-dekahertz ultraviolet spectroscopy of $^{199}Hg^{+}$," *Phys. Rev. Lett.*, vol. 85, pp. 2462–2465, Sep 2000.

[14] A. D. Ludlow, M. M. Boyd, J. Ye, E. Peik, and P. O. Schmidt, "Optical atomic clocks," *Rev. Mod. Phys.*, vol. 87, pp. 637–701, Jun 2015.

[15] T. Rosenband, P. O. Schmidt, D. B. Hume, W. M. Itano, T. M. Fortier, J. E. Stalnaker, K. Kim, S. A. Diddams, J. C. J. Koelemeij, J. C. Bergquist, and D. J. Wineland, "Observation of the $^1S_0 \rightarrow ^3 P_0$ clock transition in $^{27}Al^{+}$," *Phys. Rev. Lett.*, vol. 98, p. 220801, May 2007.

[16] T. Rosenband, D. B. Hume, P. O. Schmidt, C. W. Chou, A. Brusch, L. Lorini, W. H. Oskay, R. E. Drullinger, T. M. Fortier, J. E. Stalnaker, S. A. Diddams, W. C. Swann, N. R. Newbury, W. M. Itano, D. J. Wineland, and J. C. Bergquist, "Frequency Ratio of Al^{+} and Hg^{+} Single-Ion Optical Clocks; Metrology at the 17th Decimal Place," *Science*, vol. 319, no. 5871, pp. 1808–1812, 2008.

[17] N. Huntemann, B. Lipphardt, C. Tamm, V. Gerginov, S. Weyers, and E. Peik, "Improved limit on a temporal variation of m_p/m_e from comparisons of Yb^+ and Cs atomic clocks," *Phys. Rev. Lett.*, vol. 113, p. 210802, Nov 2014.

[18] M. S. Safronova, V. A. Dzuba, V. V. Flambaum, U. I. Safronova, S. G. Porsev, and M. G. Kozlov, "Highly charged ions for atomic clocks, quantum information, and search for α variation," *Phys. Rev. Lett.*, vol. 113, p. 030801, Jul 2014.

[19] M. G. Kozlov, M. S. Safronova, J. R. Crespo López-Urrutia, and P. O. Schmidt, "Highly charged ions: Optical clocks and applications in fundamental physics," *Rev. Mod. Phys.*, vol. 90, p. 045005, Dec 2018.

[20] J. C. Berengut, V. A. Dzuba, and V. V. Flambaum, "Enhanced laboratory sensitivity to variation of the fine-structure constant using highly charged ions," *Phys. Rev. Lett.*, vol. 105, p. 120801, Sep 2010.

[21] P. Micke *PhD Thesis, in preparation.*

[22] P. Micke, T. Leopold, S. King, L. Benkler, L. Spieß, L. Schmöger, M. Schwarz, J. R. Crespo López-Urrutia, and P. O. Schmidt, "Coherent laser spectroscopy of highly charged ions using quantum logic," *accepted in Nature, 2019*, 2019.

[23] W. Lotz, "Electron-impact ionization cross-sections and ionization rate coefficients for atoms and ions from hydrogen to calcium," *Z. Phys.*, vol. 216, pp. 241–247, Jun 1968.

[24] A. K. F. Haque, M. Shahjahan, M. A. Uddin, M. A. R. Patoary, A. K. Basak, B. C. Saha, and F. B. Malik, "Generalized Kolbenstvedt model for electron impact ionization of the K-, L- and M-shell ions," *Phys. Scr.*, vol. 81, p. 045301, mar 2010.

[25] Y. S. Kim and R. H. Pratt, "Direct radiative recombination of electrons with atomic ions: Cross sections and rate coefficients," *Phys. Rev. A*, vol. 27, pp. 2913–2924, Jun 1983.

[26] V. I. Fisher, Y. V. Ralchenko, V. A. Bernshtam, A. Goldgirsh, Y. Maron, L. A. Vainshtein, I. Bray, and H. Golten, "Electron-impact-excitation cross sections of hydrogenlike ions," *Phys. Rev. A*, vol. 55, pp. 329–334, Jan 1997.

[27] A. Müller and E. Salzborn, "Scaling of cross sections for multiple electron transfer to highly charged ions colliding with atoms and molecules," *Phys. Lett. A*, vol. 62, no. 6, pp. 391 – 394, 1977.

[28] B. M. Penetrante, J. N. Bardsley, D. DeWitt, M. Clark, and D. Schneider, "Evolution of ion-charge-state distributions in an electron-beam ion trap," *Phys. Rev. A*, vol. 43, pp. 4861–4872, May 1991.

[29] R. Marrs, "Self-cooling of highly charged ions during extraction from electron beam ion sources and traps," *Nucl. Instrum. Methods Phys. Res. B*, vol. 149, no. 1, pp. 182 – 194, 1999.

[30] L. Schmöger, "Ein elektrodynamisches System für den Transfer hochgeladener Ionen in eine Paulfalle," *Diploma Thesis, Ruprecht-Karls-Universität, Heidelberg*, 2013.

[31] L. Schmöger, "Kalte hochgeladene Ionen für Frequenzmetrologie," *PhD Thesis, Ruprecht-Karls-Universität, Heidelberg*, 2017.

[32] J. Stark *PhD Thesis, in preparation.*

[33] J. Stark, "Design ultrastabiler Hochfrequenzfelder für die Langzeitspeicherung hochgeladener Ionen," *Master Thesis, Ruprecht-Karls-Universität, Heidelberg*, 2015.

[34] P. Micke, S. Kühn, L. Buchauer, J. R. Harries, T. M. Bücking, K. Blaum, A. Cieluch, A. Egl, D. Hollain, S. Kraemer, T. Pfeifer, P. O. Schmidt, R. X. Schüssler, C. Schweiger, T. Stöhlker, S. Sturm, R. N. Wolf, S. Bernitt, and J. R. Crespo López-Urrutia, "The heidelberg compact electron beam ion traps," *Rev. Sci. Instrum.*, vol. 89, no. 6, p. 063109, 2018.

[35] L. Schmöger, M. Schwarz, T. M. Baumann, O. O. Versolato, B. Piest, T. Pfeifer, J. Ullrich, P. O. Schmidt, and J. R. Crespo López-Urrutia, "Deceleration, precooling, and multi-pass stopping of highly charged ions in Be^+ coulomb crystals," *Rev. Sci. Instrum.*, vol. 86, no. 10, p. 103111, 2015.

[36] H. Kreckel, H. Bruhns, K. A. Miller, E. Wåhlin, A. Davis, S. Höckh, and D. W. Savin, "A simple double-focusing electrostatic ion beam deflector," *Rev. Sci. Instrum.*, vol. 81, no. 6, p. 063304, 2010.

[37] K. Blaum and S. George, "Stored charged particles - Precision experiments with stored and cooled particles," *lecture notes*, 2017.

[38] A. Kramida, Yu. Ralchenko, J. Reader, and the NIST ASD Team, "Nist atomic spectra database (ver. 5.7)." Available: `https://physics.nist.gov/asd` [2017, Apr] NIST, Gaithersburg, MD., 2019.

[39] M. Hellsing, L. Karlsson, H. O. Andren, and H. Norden, "Performance of a microchannel plate ion detector in the energy range 3-25 keV," *Meas. Sci. Technol.*, vol. 18, pp. 920–925, Nov 1985.

[40] A. Egl, I. Arapoglou, M. Höcker, K. König, T. Ratajczyk, T. Sailer, B. Tu, A. Weigel, K. Blaum, W. Nörtershäuser, and S. Sturm, "Application of the continuous stern-gerlach effect for laser spectroscopy of the $^{40}Ar^{13+}$ fine structure in a penning trap," *Phys. Rev. Lett.*, vol. 123, p. 123001, Sep 2019.

[41] V. Mäckel, R. Klawitter, G. Brenner, J. R. Crespo López-Urrutia, and J. Ullrich, "Laser spectroscopy on forbidden transitions in trapped highly charged Ar^{13+} ions," *Phys. Rev. Lett.*, vol. 107, p. 143002, Sep 2011.

[42] J. Nauta, A. Borodin, H. B. Ledwa, J. Stark, M. Schwarz, L. Schmöger, P. Micke, J. R. C. López-Urrutia, and T. Pfeifer, "Towards precision measurements on highly charged ions using a high harmonic generation frequency comb," *Nucl. Instrum. Methods Phys. Res. B*, vol. 408, pp. 285 – 288, 2017.

Appendix A

Acknowledgments

I am obliged to thank the Ruprecht-Karls-Universität Heidelberg and the Max-Planck-Institut für Kernphysik for the opportunity to do my masters programs. Additionally I'd like to thank the whole EBIT-Group, not only for sharing their knowledge with me, but also for providing a friendly and motivating work climate.
My special thanks are due to:

Priv.-Doz. Dr. José Ramón Crespo López-Urrutia, for providing me with the opportunity to work on this master thesis in his group and his guidance throughout the project.

Prof. Dr. Klaus Blaum, for taking my oral master examination and agreeing to be the second examiner of this thesis.

Steffen Kühn, for supervising this project and helping me with the small day-to-day problems that arose in the course of this thesis.

Dr. Keisuke Fujii, for providing the initial measurement script that evolved into the data acquisition ultimately used, and his assistance in the laboratory

Moto Togawa & Sungnam Park, for their support in the laboratory.

Peter Micke, for minutely answering any questions regarding the beamline design, implementation or operation.

The remaining CryPTEx-II group, for the successful cooperation on the whole project.

The main Workshop, for producing the parts for this experiment.

The workshop of Christian Kaiser, for adjusting unfitting components, at times on a daily basis.

The PENTATRAP group & the CryPTEx-I experiment, for temporarily providing crucial equipment that would not have been available at the time.

Appendix B

Deposition

Erklärung:

Ich versichere, dass ich diese Arbeit selbstständig verfasst habe und keine anderen als die angegebenen Quellen und Hilfsmittel benutzt habe.

Heidelberg, 5. November 2019

. . . . . .

Michael Karl Rosner